UNIVERSITY OF MINNESOTA

This is to certify that I have examined this copy of a master's thesis by

Bhairavi Shankar

and have found that it is complete and satisfactory in all respects,
and that any and all revisions by the final
examining committee have been made.

Vicki L. Hansen

Name of Faculty Adviser

Signature of Faculty Adviser

Date

GRADUATE SCHOOL

A GLOBAL SURVEY OF CIRCULAR LOWS: A SUBSET OF CORONAE, VENUS

**A THESIS
SUBMITTED TO THE FACULTY OF THE GRADUATE SCHOOL
OF THE UNIVERSITY OF MINNESOTA
BY**

BHAIRAVI SHANKAR

**IN PARTIAL FULFILLMENT OF THE REQUIREMENTS
FOR THE DEGREE OF
MASTER OF SCIENCE**

VICKI L. HANSEN

JULY 2008

Dedication

To my grandparents, parents, and mentors who encouraged me to reach for the stars.

Abstract

Venus's coronae are quasi-circular features ranging from 60 to 1010 km with varying morphology displaying evidence of tectonic and volcanic activity. Coronae occur in chains at middle elevations (60%), clusters associated with volcanic rises in the highlands (30%), or individually within the lowlands (10%). Coronae are presumed, by most workers, to originate from the endogenic rise of buoyant diapirs. An alternate hypothesis suggests coronae are modified impact craters, products of exogenic process. Models of rising diapirs predict radial structures to form early on overlying lithosphere as it reshapes into domes, masking the interaction of low density diapirs with surface layers. However, many coronae form depressions instead of domes and many lack radial structures. The absence of predicted radial features does not explain the formation of a subset of coronae – amphitheatre sized circular depressions called circular lows.

A global study of circular lows sheds light on their mode(s) of formation. I catalogue the position of circular lows and characterize them in order to test the two major hypotheses of coronae formation. Using synthetic aperture radar (SAR) and altimetry data from the NASA Magellan mission (1991 – 1994), the global survey found 55 circular lows, distributed across the planet (excluding the polar areas due to lack of necessary data) and range in diameter from ~70 to 450 km. The basins are circular to quasi-circular features with mean ellipticity of 0.9. Circular lows are shallow features with depths less than or equal to 2.55 km and typically display a rim, closely spaced annulus, and lack radial structures. Circular lows occur individually and dominate the lowland regions of the planet.

The characteristics of circular lows and the proximity of circular lows to ancient tessera terrain are more consistent with formation due to either bolide impact, or surface expressions of subsurface subsidence. This work ultimately adds a new dimension to understanding the dynamics of endothermic and/or exothermic processes on Venus.

Table of Contents

Introduction:

The surface of Venus consists of many circular structures including large volcanic rises, crustal plateaus, coronae and impact craters. Corona(e), a Latin term for *crown*, are quasi-circular features that range in diameter from 60 to 1010 km with a median of ~200 km. The 515 recorded coronae occur in chains within the mesoland (60%), as clusters associated with volcanic rises in the highland (30%), or individually within the lowlands (10%) (Stofan et al., 1992; Smrekar and Stofan, 1997). Coronae vary in morphology including domes, plateaus, depressions, rings, and lacking distinct topographic signature. Coronae show varying evidence of volcanic activity, as well as tectonic features.

Most workers accept the hypothesis that all coronae represent the surface signatures of mantle derived buoyant diapirs that interacted with the upper crust (Stofan et al., 1991, 1992, 1997; Janes et al., 1992; Squyres et al., 1992; Smrekar and Stofan, 1997). The widely variable characteristics of coronae suggest that: 1) many stages of coronae formation are preserved, 2) coronae are formed by more than one mechanism, or 3) both. Through different stages of diapir evolution and ultimate dissipation of thermal buoyancy, the surface responded in varied ways producing the observed topographic and geologic characteristics. By this mechanism, coronae may be an endogenic mechanism by which Venus loses internal heat and cools. Numerical, experimental and finite-element models predict circular basins might form at the final stage of buoyant diapir evolution when the overlying surface relaxes gravitationally (Withjack and Scheiner, 1982; Cyr and Melosh, 1993; Koch and Manga, 1996).

A second hypothesis states that all coronae mark bolide impact craters (Vita-Finzi et al., 2005; Hamilton, 2005). According to this hypothesis, impact craters, circular

basins surrounded by a rim and ejecta blanket, evolve to become corona through surface modification. According to this hypothesis, coronae represent exogenic features, and as such, would indicate that Venus' surface is older than currently accepted.

Although these two hypotheses present opposing ways in which coronae form, both predict the formation of circular depressions. A morphological subset of coronae with amphitheatre-sized depressions, called circular lows, forms the focus of this study. Not much has been stated in the literature regarding the locations and structural characteristics of circular lows. McDaniel (2005) constructed detailed geologic maps of five coronae that display interior circular basins. She proposed that although coronae in general may result from an endogenic (diapir) process, the five features she mapped might be products of exogenic bolide impacts rather than endogenic processes.

I conducted a global survey of coronae marked with circular basins, herein called circular lows, using NASA Magellan synthetic aperture radar (SAR) and altimetry data in order to better define circular low characteristics. Structures predicted from each hypothesis have been compared to structures associated with circular lows to resolve the question regarding how circular low, collectively and/or individually, may form. If structural evidence supports a diapiric origin for circular lows, there are implications on the heat transfer and cooling of the planet. If circular lows represent products of bolide impacts, the difference between circular lows and Venus's well documented pristine impact craters needs to be addressed. The evolution of diapiric features needs to accommodate critical relations identified through the global survey of circular lows. Examining circular lows independently allows a better assessment of the existing hypotheses regarding their mode of formation.

The global survey, using NASA Magellan synthetic aperture radar (SAR) and altimetry data, yielded 55 circular lows located between 75°N and 75°S. Circular lows: dominate the lowland areas of the planet, occur as isolated circular features, display closely-spaced concentric structures, lack radial structures, and lie within relatively close proximity to tessera terrain. As will be shown, these general characteristics of circular lows are difficult to justify within a diapiric evolutionary process and are most consistent with formation by: bolide impact, caldera collapse, and/or subsurface processes involving either negatively buoyant diapirs, or material transfer most likely as liquids.

Background:

Venus

Venus, considered Earth's sister planet, is comparable to Earth in size, density, and distance from the Sun [Table 1]. Therefore it is assumed that the bulk composition and cooling history of Venus would be similar to that of Earth but Venus evolved differently, developing different structures than Earth. Venus: 1) rotates in a retrograde manner with a day longer than a year (243 versus 224 Earth days); 2) has a surface temperature of ~750K (475°C); 3) has an atmosphere of 96% CO_2 and 3% N_2; 4) an atmospheric pressure of ~92 atm; and 5) Venus lacks water. The hypsometric curve of Earth displays bimodal crustal distribution (granite-rich continental crust and basaltic oceanic crust), yet the hypsometric curve of Venus indicates a unimodal distribution of basaltic crust (Barsukov et al., 1982). Earth loses internal heat through plate tectonic movements, marked on the surface by linear features such as subduction zones, spreading center ridges and transform faults; Venus, however, lacks any evidence of plate movement. The Venusian surface displays numerous circular features that show evidence of both volcanic and tectonic activity. Images collected by the NASA Magellan mission show large circular features on Venus including volcanic rises (1000 to 2400 km in diameter), crustal plateaus (1500 to 2500 km in diameter), coronae (60 to 1010 km in diameter), impact craters (1.5 to 270 km in diameter), and small shield edifices (< 10 km in diameter) (Schaber et al., 1992; Stofan et al., 1992). Two circular features on Venus, coronae and impact craters, are discussed in this paper. Topographically, *lowlands* are regions lower than the mean planetary radius of 6051.8 km; *highlands* are regions higher than the mean planetary radius by at least two kilometers; and regions that lie between

4

Table 1. Physical characteristics of Earth and Venus.

	Earth	Venus
Distance from Sun	1 AU (1.496×10^8 km)	0.72 AU (1.082×10^8 km)
Orbit Eccentricity	0.017	0.0068
Planetary radius (km)	6378	6051.8
Mass (kg)	5.974×10^{24}	4.869×10^{24}
Mean Density (kg/m^3)	5515	5240
Surface Gravity	1	0.91
Orbital period (days)	365	224
Rotational period (days)	1 (24 hours)	243 (retrograde)
Surface Temperature (^{o}C)	25	475
Atmosphere Composition	77% N_2, 22% O_2	96% CO_2 , 3% N_2
Atmospheric Pressure (bars)	1	92

the lowland and highland are considered the *mesolands* (Phillips and Hansen, 1994).

Volcanic plains, generally lowlands, make up about 80% of the planet, and the remaining

20% are mesoland regions (10 – 12%) and highland regions (8 – 10%) dominated by

ancient ridge *tessera* terrain, volcanic rises, and crustal plateaus (Saunders et al., 1992).

NASA Magellan Mission

The NASA Magellan mission (1990-1994) collected globally-extensive radar

images of Venus. Across five mapping cycles, the mission collected: 1) synthetic-

aperture radar (SAR), 2) emissivity, 3) altimetry, and 4) gravity data. The first three

mapping cycles collected SAR images at a resolution of 120 m/pixel, and a near global

topographic dataset with a horizontal resolution of 10 km and a vertical resolution of 80

m (Ford et al, 1993). These data allow an integrated study of the surface and near

subsurface of Venus. Magellan datasets used in the study of circular basins are discussed

further in the data section.

Coronae

Corona(e), Latin for *crown*, are quasi-circular features dominant on Venus that

display a wide range of morphology, annuli, and deformed surroundings (Stofan et al.,

1991, 1992, 1997; Janes et al., 1992; Smrekar and Stofan, 1997). The 515 recorded

coronae on Venus range in diameter from 60 to 1010 km, with a median size of 200 km.

Coronae morphology includes domes, plateaus, depressions, and rims [Fig. 1]. Coronae

occur in chains (60%), clusters (30%), or isolated from other geologic features (10%)

(Stofan et al., 1992, Stofan and Smrekar, 1997).   Coronae typically display radial
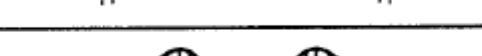
Group	Topographic profile	Description	% of coronae
1		Dome	10
2		Plateau	10
3a		Rim surrounding interior high	21 (a+b)
3b		Rim surrounding interior dome	
4		Rim surrounding depression	25
5		Outer rise, trough, rim, inner high	5
6		Outer rise, trough, rim, inner low	1
7		Rim only	7
8		Depression	7
9		No discernible signature	14

Figure 1. Topographic profiles of various coronae morphologies with annuli marked as vertical tick marks (after Smerkar and Stofan, 1997). There are 515 coronae on Venus. Groups 4 and 8 (circled) display circular basins (~165 in number) – features I classify as circular lows.

7

fractures and circular bands (annuli) of fractures and/or ridges. Regional tectonic activity on coronae is recorded in the annuli. Smooth deposits from exterior flows and individual shields (2 to 20 km in diameter) strongly suggest volcanic activity associated with many coronae (Basilevsky et al., 1986; Stofan et al., 1992; Janes et al., 1992). Coronae are further classified as Type-1 or Type-2 coronae (Stofan et al., 2001). Type-1 coronae, a group of 105 coronae, display complete or nearly complete annuli. The remaining 410 coronae, termed Type-2 coronae, have less than 50% complete annuli. Type-2 coronae typically occur in the lowlands and have flat or depressed interiors.

Most researchers favor an endogenic (diapir) mode of formation of coronae, attributing various coronae morphologies to varying stages of corona evolution. However the wide range in morphologies and size suggests that more than one process may be responsible for corona formation. Circular basins, herein called circular lows, are a morphological subset of coronae and form the focus of this study. Addressing the role of diapirs in forming circular lows along with other hypotheses is further addressed in the hypotheses section.

Impact Craters

Approximately 970 impact craters are distributed across Venus in a near spatially random pattern, with a mean planetary crater density of about two craters per $10^6 \, km^2$ (Schaber et al., 1992). Impact craters vary in morphology and range in diameter (1.5 to 270 km, 10 km median) (Phillips et al., 1992; Schaber et al., 1992; Herrick et al., 1997). Depths of impact craters range from 0.2 to 1.0 km (Schaber et al., 1992). In general, impact craters are defined by: 1) circular depressions, 2) raised rims, 3) ejecta deposits

8

that enclose the rims, and 4) locally radar smooth or rough halos (Schaber et al., 1992; Herrick and Phillips, 1994). Impact craters are pristine (62%), affected by tectonism (32%), or, rarely, embayed by volcanic flows (4%) (Schaber et al., 1992) [Fig. 2]. Although the majority of impact craters are pristine, some appear degraded due to volcanism, tectonism, and/or alteration resulting from high temperatures at the surface. With increasing age, crater halos and ejecta eventually disappear (Izenberg et al., 1994). Stages of impact crater degradation are illustrated in Figure 3.

Circular Lows

Circular lows are a subset of coronae with a topographically low interior surrounded by a rim and annulus. McDaniel (2005) constructed detailed geologic maps of five circular lows, using the available NASA Magellan SAR images and altimetry data. Four of the five circular lows are adjacent to ribbon tessera terrain, ancient terrain that is well preserved on Venus. McDaniel (2005) suggested that the geologic characteristics and recorded geologic histories of the five targeted circular lows may be more consistent with formation via bolide impact.

a)

b)

c)

d)
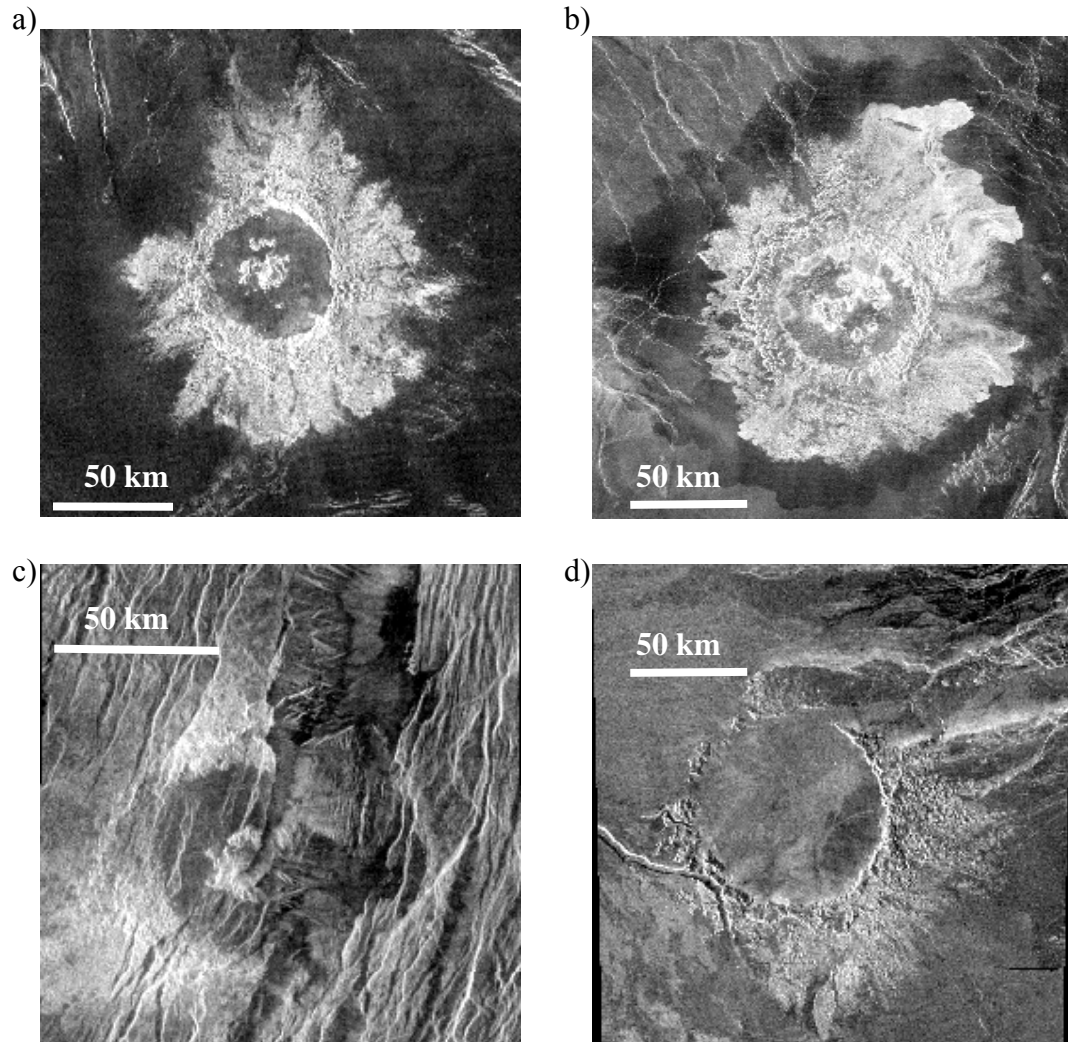
Figure 2. Magellan SAR images of representative impact craters. Craters appear
pristine, embayed, or affected by tectonism.
a) "Pristine" Danilova Crater (26.4^{o}S/ 337.2^{o}E) with a central peak in the interior.
b) "Pristine" Yablochkina Crater (48.3^{o}N/ 195.15^{o}E) with a radar dark halo and radar
bright outflow deposits.
c) "Tectonized" Balch Crater (29.9^{o}N/ 282.90^{o}E) cut by NNE-striking fractures and
faults.
d) "Embayed" Alcott crater (59.50^{o}S/ 354.55^{o}E), extensively flooded by lava.
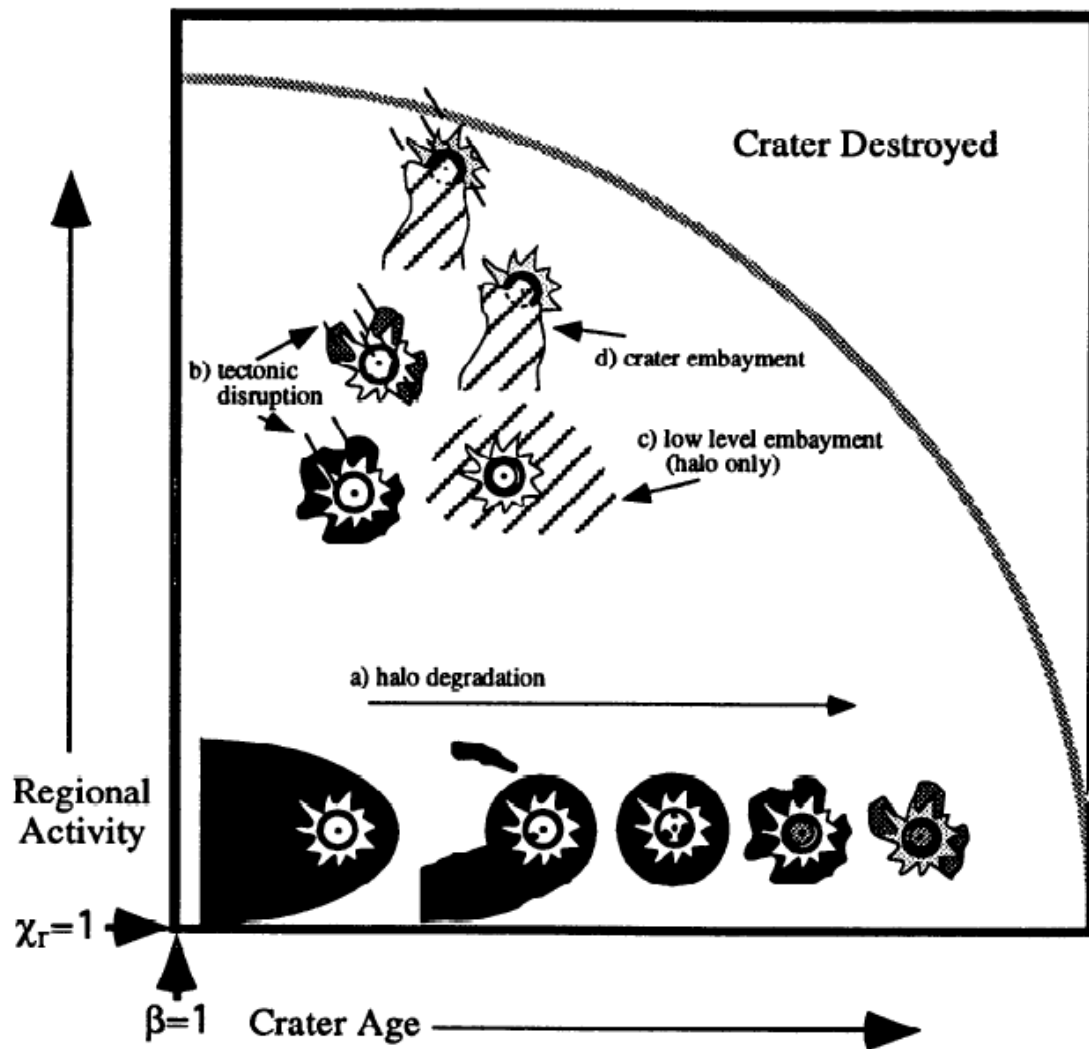
Figure 3. Crater degradation model show the effects of volcanism and tectonism on pristine impact craters (after Izenberg et al., 1994). With increasing age and regional tectonic activity, parabolas around craters degrade to halos that ultimately fade away. At extreme levels of activity, craters are either embayed, tectonized, or both.

Data

The NASA *Magellan* mission (1991-1994) collected global radiometry, emissivity, gravity, synthetic aperture radar, and altimetry datasets across 98% of the planet over five mapping cycles (Saunders et al., 1992; Ford et al., 1993). Synthetic aperture radar, altimetry, and synthetic stereo images (created by combining radar and altimetry data) data are key datasets used in the current study to examine circular lows. The Magellan sensor instrument acquired data in three modes: synthetic aperture radar (SAR), radiometer, and altimeter modes. A 3.7 m diameter parabolic high-gain antenna fixed 25° off nadir perpendicular to the trajectory of the spacecraft was used to collect data in SAR and radiometer modes [Fig. 4]. A nadir-directed altimeter horn antenna was used to collected altimeter data. The sensor sent microwave pulses and recorded the echo for all three modes (SAR, radiometer, and altimeter) in batches several times per second (burst periods). The mapping-orbit profile started from the northern polar region proceeding clockwise in a west to east direction. Data from each orbit, 20 km wide and 17,000 km long, were combined to produce mosaics. The first three mapping cycles collected SAR data and altimeter measurements. SAR images were obtained at a various resolutions ranging from 75 m/pixel (full resolution) to 125 m/pixel. Resolution varies depending on latitude and degree of compression. In cycle 1, a left-looking geometry, the high gain antenna pointed east of the spacecraft nadir track, and incidence angles varied to get most coverage. Cycle 2 has a right-looking geometry mapping with a fixed incidence to fill data gaps from cycle 1. Cycle 3 mapped stereo radar (it combined with cycle 1 data) in left-looking geometry. The last two mapping cycles collected gravity data. The datasets greatly assist in understanding the geologic nature of Venus.

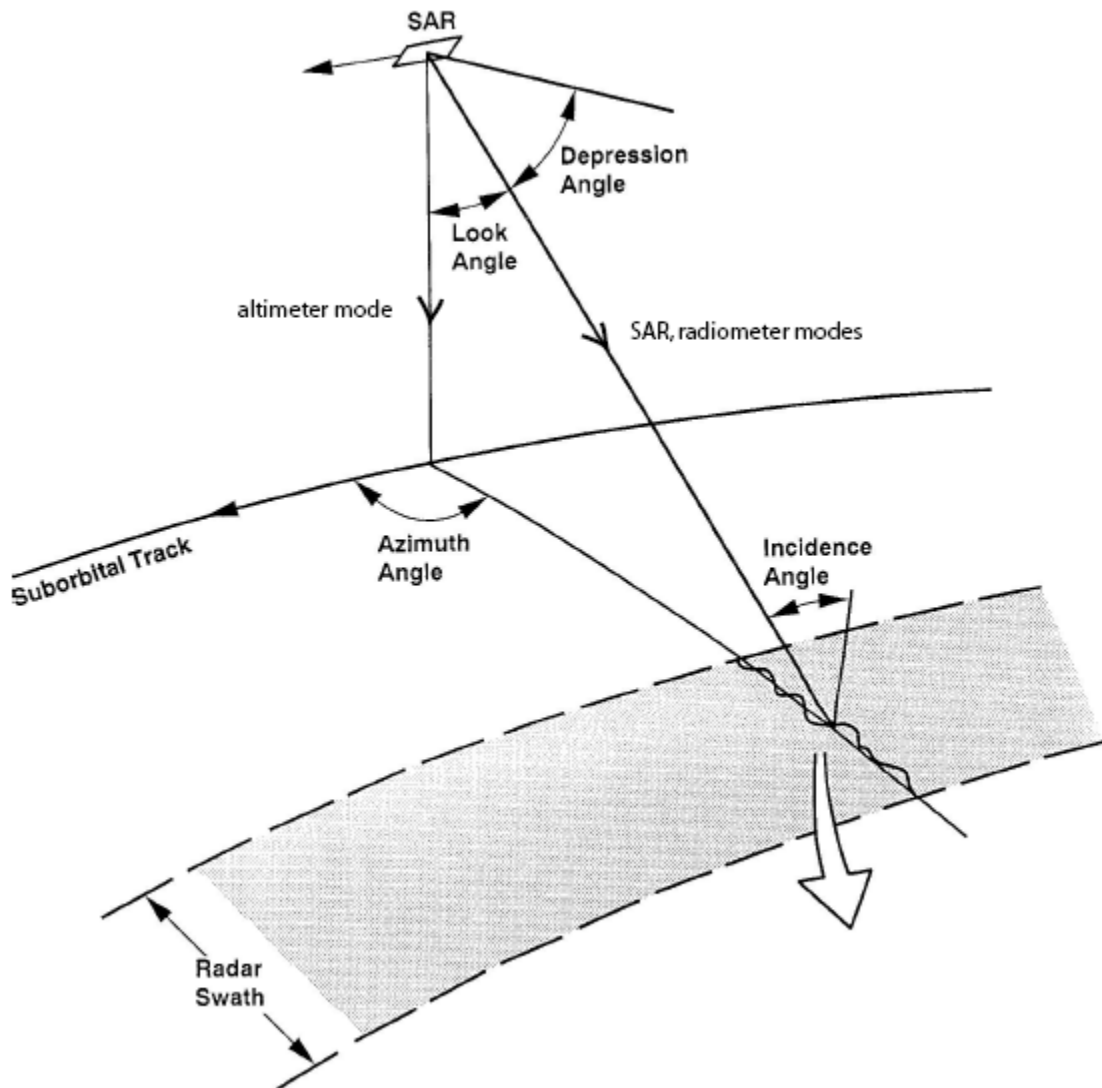Figure 4. Swath paths for radar and altimeter data image acquisition (after Farr et al., 1993). The side-look geometry of the sensor allows greater penetration of microwave signals through the thick atmosphere allowing the maximum surface to be imaged. The nadir-directed altimeter horn antenna records altimeter data. The strength of the reflected signal is dependent on surface roughness and outlined in Figure 6.

Near global topography was obtained with a horizontal resolution of 10 km and vertical resolution of ~80 m (Saunders et al., 1992; Fort et al., 1993).

Radiometry and Emissivity

Thermal radiation emitted by the planet was recorded by the high gain antenna as radiometric data during the first three cycles. The radiometer footprint (patch of surface measured) along track and a cross track are similar in size to the altimeter footprints (defined further in the altimeter section). Surface emissivity, the amount of radiation energy emitted from an object on the surface, was derived from the radiometric measurements to interpret surface roughness independent of the SAR image data. However, the mix of emissivity with SAR data makes it difficult to use emissivity data in the study of circular lows.

Gravity

The last two mapping cycles gathered gravity data, recording density variations within the planet's interior (Ford and Plaut, 1993). Gravity data are derived from the altimetry data. Coarse resolution of the Magellan gravity data makes it difficult to resolve features smaller than 400 km and therefore is not used in this study.

Altimetry

Altimetry data shows the topographic variation of the Venusian surface, including the form of circular basins. In the altimeter mode, the Magellan sensor was connected to a small nadir-directed altimeter horn antenna (ATLA) to determine the distance between

14

the spacecraft and surface. Each altimeter footprint taken by Magellan varied with the spacecraft altitude and latitude, but each was spaced approximately 8 km in the long track direction and 10 km in the cross track direction (Ford et al., 1993). A total of 1000 altimeter footprints per orbit combine to form the global topographic data record (GTDR), with horizontal resolution of ~10 km and vertical resolution of ~80 m. Reflectivity and root-mean-square slope datasets were also derived from altimeter data. Features away from a footprint point will appear distorted, and therefore they do not give accurate topographic information posing limits to the topographic data. On Venus, the elevation is measured relative to the mean planetary radius of 6051.8 km (Plaut, 1993). Topographic maps with contour lines to determine topographic profiles of individual circular lows were generated using macros developed by D. A. Young.

Synthetic Aperture Radar (SAR)

The SAR sensor operated at a wavelength of 12.6 cm at 2.385 GHz (S-band) with horizontal parallel transmit and receive polarization (HH) in order to penetrate the thick, CO_2-dominated cloud cover. Due to the elliptical orbit, the SAR incidence angle varied with latitude. SAR data were gathered during the first three cycles, each with a different looking geometry (left-look, right-look, and stereo left-look), covering ~98% of the planet surface. Because of the side-looking geometry, all radar images are, to some extent, distorted; the amount of distortion depends on latitude and resolution. The resolution of SAR images range between ~75 m/pixel (full resolution, F-MIDR) to ~225 m/pixel (compressed once, C1-MIDR) and ~675 m/pixel (compressed twice, C2-MIDR) (Senske et al., 1993), with an effective radar resolution dependent on the feature

(Zimbelman, 2001). Figure 4 illustrates the geometry of the swath path, and Table 2 summarizes the radar and orbital characteristics. The surface has been divided into 62 georeferenced cartographic maps by the U.S. Geological Survey (quadrangles or Venus maps) useful in locating features on the planet [Fig. 5]. Geologic maps of certain sections of the planet have been published at a 1:5 million scale and the status of mapping is also indicated in Figure 5.

Radar image brightness depends on the roughness and topographic properties of the imaged surface. Surfaces facing the incident radar, and/or rough surfaces in general, appear radar bright, whereas smooth surfaces (below the scale of radar wavelength) or surfaces facing away from the incident radar, appear radar dark [Fig. 6]. In the case of negative SAR images (inverted), the reverse is true, rough surfaces appear dark and smooth surfaces appear bright. Inverted SAR images are useful in structural analysis because lineaments appear better in inverted images.

Depending on the look direction of the sensor, echos off areas of high elevation return to the sensor earlier than areas of low elevation. This leads to higher elevations imaging forward of their true position, an artifact called foreshortening. If an echo from the peak returns before the echo from the forward end, the peak is imaged on top of the base; this extreme case of foreshortening is referred to as lay-over. Foreshortening and lay-over are explained further in the Appendix.

Regional and general analyses of circular lows are conducted using SAR images (225 m/pixel), altimetry data (275 m/pixel) and synthetic stereo images constructed with macros developed by D.A. Young. Full resolution SAR images at 75 m/pixel are used for detailed analysis of individual circular lows.

Table 2. Summary of the radar and altimeter characteristics
from the Magellan Mission (from Ford et al., 1993)

Radar System Characteristics	
Wavelength, cm	12.6 (S-band)
Operating frequency, GHz	2.385
Polarization	HH
Effective slant-range resolution, m	88
Along-track resolution, m	120
Usable SAR imaging orbits	4225
SAR Orbit dimensions; horizontal width, km	20
vertical length, km	17,000
Altimetry Data	
Cross-track resolution, km	8
Along-track resolution, km	10
Footprint diameter, km	10 - 30
Vertical resolution, m	80
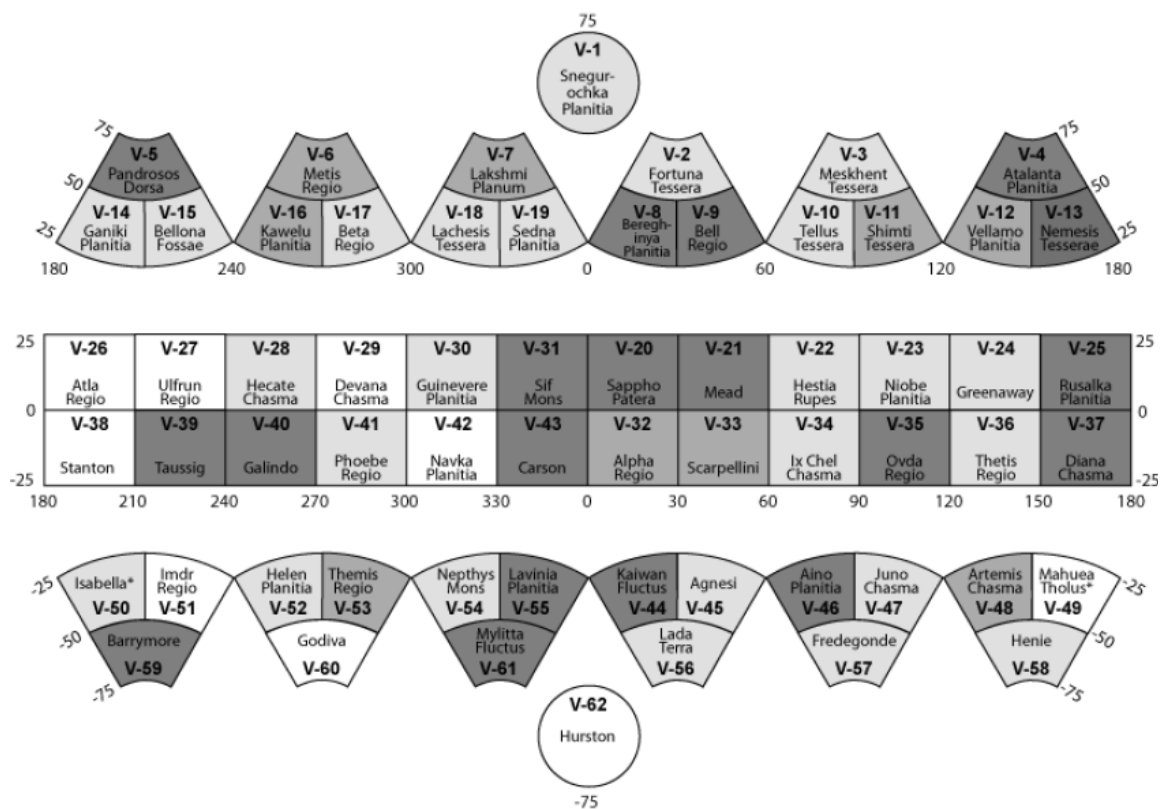
Figure 5. A 1:5 million scale cartographic representation of the Venusian surface. The
georeferenced quadrangles are used as a base for mapping. The polar regions
were projected using the polar coordinate system, equatorial quadrangles
(25ºN to 25ºS) projected using a Mercator projection system and remaining
quadrangles were mapped using the Lambert conical projection. The status of
mapping (as of 2003) is represented by the shading of each quadrangle
(Tanaka, 2003). Quadrangles in white indicate that mapping is unassigned,
light grey (ex. V-1) indicates mapping in progress. Quadrangles such as V-6,
V-7, etc. are in review and dark grey quadrangles (V-5 for example) indicate
that geologic maps have been published (from U.S. Geological Survey). Polar
regions were excluded in the global study of circular lows due to a lack of SAR
data (V-62) and synthetic stereo images.
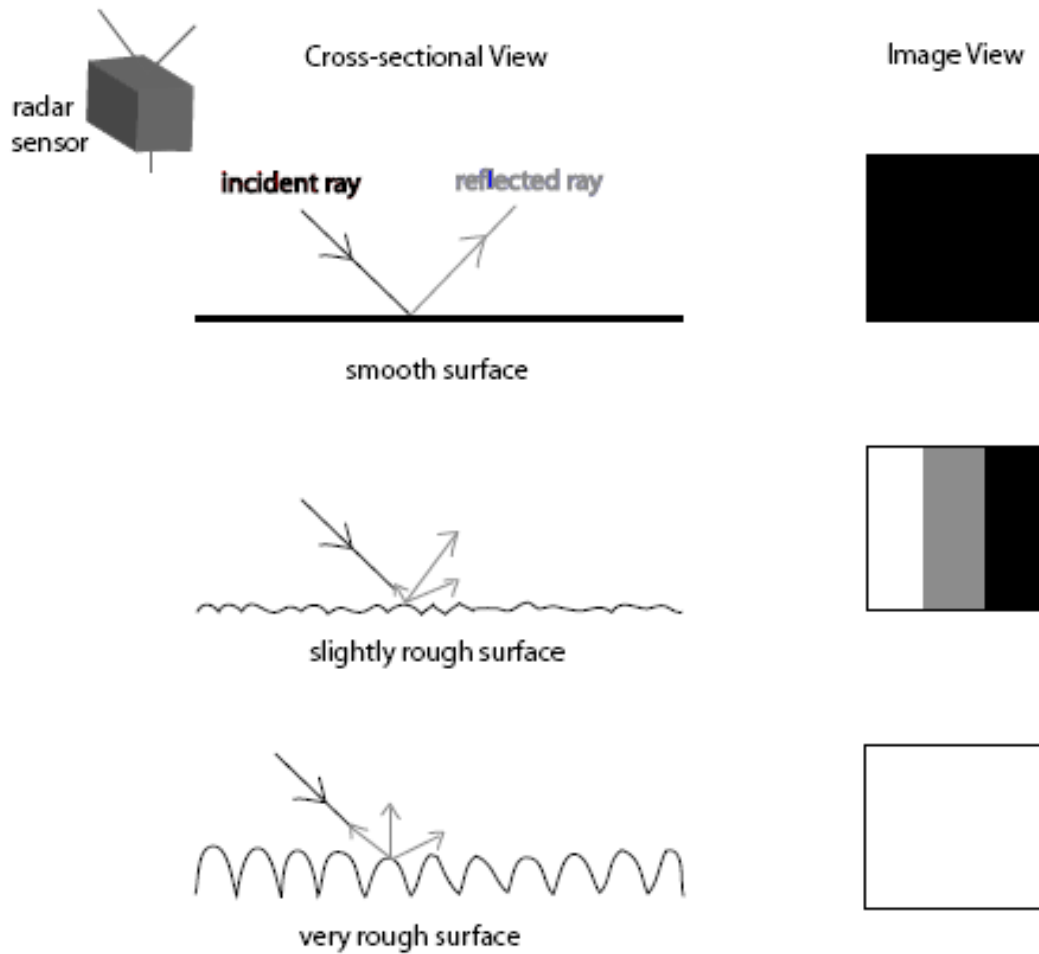
Figure 6. Reflection of radar pulses as a function of surface roughness. For a surface variation less than the radar wavelength of 12.6 cm, no energy is returned to the sensor and the area appears dark on a SAR image (top). A slightly rough surface with a variation still less than the effective radar wavelength reflects some of the incident ray back to the sensor and on an image appears grey (middle). A rough surface with the variation much greater than the effective radar wavelength reflects a significant amount of incident rays back to the sensor and therefore appears bright (bottom).

Synthetic Stereo Radar (SS)

The study of circular lows used synthetic stereo images in addition to SAR images from all three cycles (225 m/pixel resolution) and altimetry data (275 m/pixel). True stereo images are a combination of SAR data from cycles 1 and 3 (both with the same look directions but different incidence angles), and are ideal in interpreting surfaces because the combined image can be visualized in three-dimensions. Parallax differences between the two images produce a depth to the image. However, very little of the surface was imaged in cycle 3 from the Magellan mission, therefore true stereo data are available only across limited regions of the surface and, as such, could not be used in the current study. However, digital combination of SAR data (cycles 1, 2, or 3) with altimetry yields *synthetic* stereo images. Because SAR and altimetry cycles image ~98% of the planet (Kirk et al., 1992), synthetic stereo images are almost global (the polar regions, V-1 and V-62 cannot be displayed as synthetic stereo images due to their projection). A distortion is introduced from combining altimetry and SAR images. Despite lower resolution than true stereo images, regional differences in the topography and surface features are distinguishable in synthetic stereo images. Synthetic stereo images are extremely useful in the survey of circular lows. Radar brightness properties defined for SAR images in the previous section are also applicable to synthetic stereo images. The stereo pairs can be viewed as color (red-blue) anaglyphs. Red color projects the combined SAR images from both cycles, and the blue color projects the distorted image to produce a red-blue anaglyph.

Synthetic stereo images (normal and inverted) of 60 georeferenced Venus quadrangles, V-2 to V-60, were used to identify and record the geographic locations of

circular lows. Both SAR and synthetic stereo images (normal and inverted) were used in determining structural characteristics of circular lows.

Data Availability

For the study of circular lows, SAR images of the entire planet published at a 225m/pixel resolution are readily available in the Planetary Processes Lab (Department of Geological Sciences) at the University of Minnesota-Duluth in TIFF format. Full resolution SAR images are available online from the USGS Map-a-planet website (http://pdsmaps.wr.usgs.gov/) in different formats and look geometry. Synthetic stereo and SAR images of V-map quadrangles V-2 to V-61 are available at the University of Minnesota- Duluth, Department of Geological Sciences. The polar quadrangles, V-1 and V-62, were not included in the survey due to lack of available synthetic stereo images of these quadrangles. Topographic profiles and synthetic stereo images of individual circular lows are generated using macros developed by D.A. Young.

Methodology

I conducted a global survey of circular lows using Magellan altimetry data, SAR, and synthetic stereo images. Circular lows are best recognized in synthetic stereo images where regional variations of the topography, and surface features are distinguishable. For individual circular lows I determined: 1) location; 2) topographic setting; 3) spatial setting; 4) plan-form shape (ellipticity); 5) diameter; 6) topographic profiles; 7) presence, extent and character of radial and concentric structures; and 8) presence of obvious lobate flows. Observations of features such as pancake domes emerged during the study and are also included in the dataset. I also compared locations and characteristics of circular lows with one another and with other global databases including: 1) global topographic data, 2) impact craters, and 3) global tessera terrain (ancient terrain) distribution.

I recorded the geographic location and mapped basic geologic structures within and around individual circular lows by linking georeferenced SAR and synthetic stereo images using Adobe Illustrator CS2™ running in a Windows environment with a Wacom Cintiq 21X LCD write-on tablet. MAPublisher 6.2™, a plug-in for Adobe Illustrator™, is used to convert digitized circular lows to an ArcGIS™ environment to determine spatial and topographic settings.

Global trends of circular lows relative to other global databases are analyzed using the ArcGIS™ Globe feature. Other global datasets that have been independently compiled include: impact craters (Herrick et al., 1997), global altimetry, deformation belts, spatial settings of coronae (Stofan et al., 1992), and ancient tessera terrain (Hansen and Lopez, 2008).

I conducted a global survey, looking at synthetic stereo images of 60 georeferenced V-Map quadrangles (V-2 to V-61) to determine the location and number of circular lows on Venus. Circular lows included in the preliminary database were identified as quasi-circular features with amphitheatre-type depressions, and free from complexity resulting from other geologic processes in the surrounding areas. The geographic locations of individual circular lows were determined using georeferenced SAR and synthetic stereo images linked in Adobe Illustrator CS2^{TM}. A total of 112 circular lows with diameter defined by the drop in slope were identified [Fig 7a]. Circular lows with large effective radar resolution were included to avoid distortion issues resulting from resolution limitations of altimetry data. Features with large effective radar resolution show more detail (Senske et al., 1993). This condition further filtered the original dataset down to 65 circular lows and the ellipticity, ratio of diameters along the short and long axes, was quantified in each case [Fig. 7a]. In order to maintain the criteria of being circular depressions, features with ellipticity less than 0.60 were excluded. The final complete dataset includes 55 circular lows for which remaining measurements and observations were made.

Observations and measurements recorded for the 55 circular lows included: 1) depth; 2) rim height; 3) spatial setting; 4) topographic setting; 5) proximity to ancient tessera terrain; 6) annuli structure data including structure type, width, location relative to the circular low, and degree of spread around circular low; 7) radial structure data including structure type, degree spread around the circular low, location of radial structures relative to the circular low, and extent of structures onto the surrounding terrain; 8) presence of lobate flows associated with the circular low; 9) structures

23

a)   plane-form view

$r_l = 1/2 \ D_l$

$e = r_s / \ r_l$

r_s
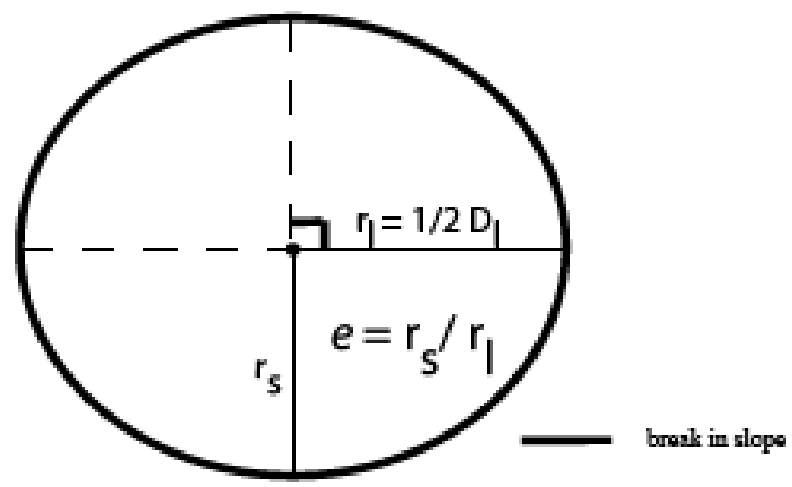
—— break in slope

b)   cross-section view

h

r_l

d

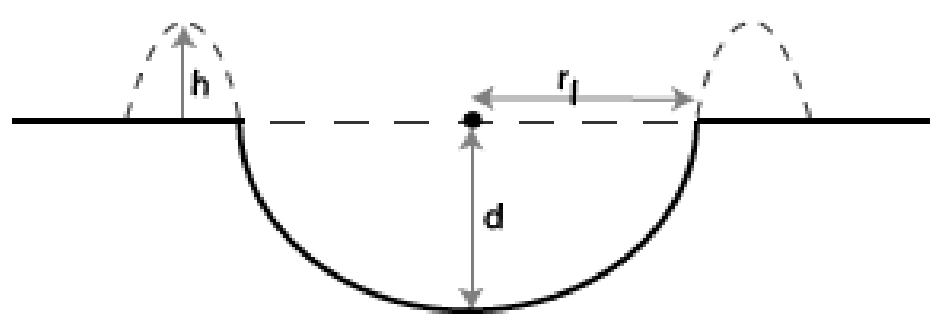Fig 7. a) Illustration showing shape characteristics of circular lows. The
        diameter (Dl) is defined by the maximum break in slope along
        the long and short axes and measured in km. Ellipticity is the ratio
        of short to long axis.

    b) Depth (d) and rim height (h) measurements of circular lows in km
       units.

and/or geologic features within the circular low interior; and 10) location of pancake domes relative to the circular low.

Global GTDR data were used to generate topographic maps (with 100 m contour interval) of individual circular lows in order to determine the depth and rim heights for circular lows [Fig. 7b]. Depth is defined as the difference between the average height of surrounding region and the lowest elevation within the basin. Rim height is defined as the difference between the highest elevation of the rim and the average height of the surrounding region. GTDR data were also used to determine the topographic setting of each circular low using ArcGIS™ Globe; circular lows are located either in the highland, mesoland, or lowland areas of the planet.

The spatial settings of individual circular lows are defined according to the spatial settings of coronae. Coronae occur in chains (60%), clusters (30%), or isolated from other geologic features (10%) (Stofan et al., 1992, Stofan and Smrekar, 1997). Determining the spatial settings of circular lows allows for comparison to coronae. MAPublisher 6.2™, a plug-in for Adobe Illustrator™, was used to convert digitized circular lows to an ArcGIS™ environment to determine spatial and topographic settings.

The proximity of individual circular lows to ancient ribbon-tessera terrain is useful to note in order to evaluate and determine the mode of formation of circular lows. As part of an ongoing independent global investigation of Venus, a complete map of ribbon-tessera terrain is currently being generated using SAR images and altimetry data (225 m/pixel and 275 m/pixel resolutions respectively), full resolution images at 75 m/pixel (Hansen and Lopez, 2008), and will be used to analyze circular lows. I

considered a circular low as adjacent to ribbon-tessera terrain if the documented ribbon-tessera terrain lies within at least a diameter length around a circular low.

Annuli characteristics recorded for individual circular lows include: 1) structure type, 2) maximum width, 3) maximum extent, 4) degree spread around circular low, and 5) location relative to the circular low [Fig. 8]. Concentric structures include troughs (fractures) and ridges (folds). For structures of ambiguous structural signatures the term lineament was used. Annuli may be located either within the interior, outside the circular low, or both. The degree spread of annuli around the circular low was recorded (θ_C). The distance from the centre of the circular lows to the closest annulus structure was also recorded (r_C). Maximum width of annuli (C_w) is defined as the total distance, from the annulus band closest to center of the circular low to the annulus extending out farthest into the surrounding surface [Fig. 8].

Radial feature characteristics recorded include: 1) maximum extent of radial structures from the centre of the circular low (r_R), 2) maximum degree spread around the circular low (θ_R), and 3) the location of radial structures relative to circular low. Radial structures may: 1) occur locally within the interior of the circular low, 2) span the whole area of the circular low but truncating at the edge, or 3) extend far beyond the circular low into the surrounding surface.

Other structures or other geologic features may spatially associate with individual circular lows, including: shields, lobate flows, pit chains, impact craters, fractures, folds, ribbons, and wrinkle ridges. These features are defined in the terminology section. In the case that geologic maps of regions are published and readily available [Fig. 5], the structural and regional information for the circular lows were obtained. The presence of
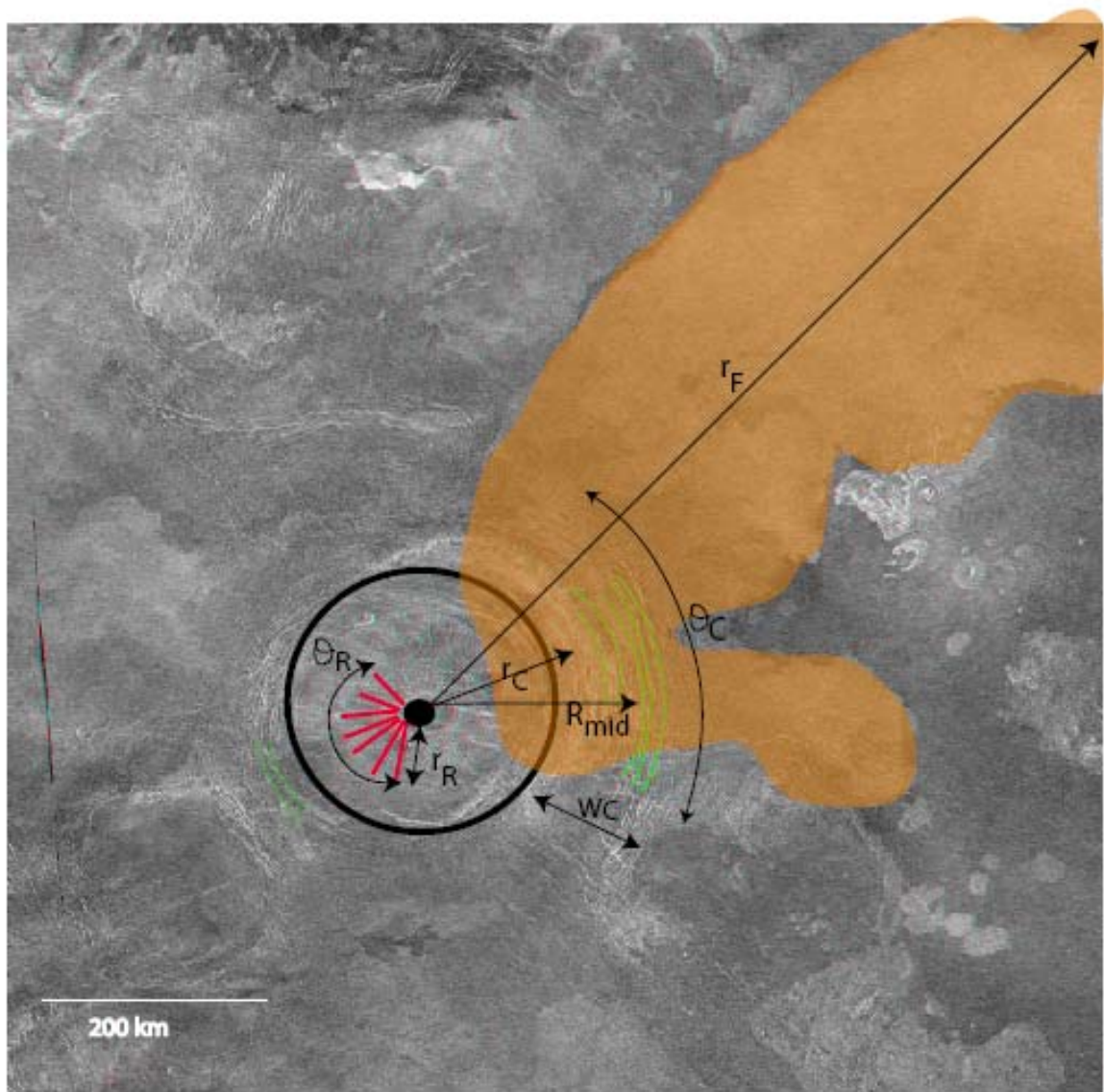
Figure 8. Synthetic stereo image of Madderakka Corona (9°N, 315.5°E) annotated with the structural characteristics recorded for circular lows including: 1) total width of annuli structures (W$_C$), 2) total distance from the centre of the circular low to the nearest annuli structure (r$_C$), R$_{mid}$ is the midpoint of the width of concentric structures.
3) maximum degree spread of concentric and radial structures around the circular low (Θ$_C$,Θ$_R$).
4) maximum extent of radial structures (r$_R$), 5) maximum extent of lobate flows associated with a circular low (r$_F$), and 6) location of characteristic features relative to the circular low (interior, exterior, or both).

27

central peaks, rims, flows, and characteristics such as surface roughness within the interior of circular lows were also recorded.

Steep-sided domes (pancake domes) were observed through the course of this study and their locations relative to the circular lows were recorded. Pancake domes lie: 1) within the interior, 2) outside in the surrounding surfaces, or 3) along the edges of circular lows.

Terminology (in alphabetical order)

The following are terms used to describe structures and topography of circular lows

i) Topographic Terms:

Depth: the height of a circular basin defined by the change in elevation of the basin floor relative to the average surrounding elevation [Fig. 7b].

Diameter: defined topographically by the maximum change in slope of the circular basin along the long axis [Fig. 7a].

Maximum change in slope: where the break in rim slope is greatest.

Ellipticity: ratio of radii of the minor and major axes [Fig. 7a].

Topographic Setting: topographic location: highland, mesoland, and lowland.

Spatial Setting: the position of circular lows relative to the spatial distribution of other coronae; that is, in chains, clusters or isolated (Stofan et al., 1992; Stofan and Smrekar, 1997).

ii) Structural Terms:

Annuli: concentric structures that surround a feature [Fig. 8].

Central Peak: topographic rise in basin interior.

Folds: ridge-type topographic lineament, interpreted as contractional structure (fold) (Stofan et al., 1993).

Fractures: narrow lineaments with trough-type topography. Fractures are interpreted as extensional structures (Stofan et al., 1993).

Interior: the inner area of a circular low; defined by topography.

Lineaments: linear features with ambiguous character (i.e. trough or ridge).

29

Lobate Flows: flows originating from a common volcanic centre radiating outwards in

        lobes.

Pancake Dome: steep sided domes with flat tops (<10 km diameters) (Head et al., 1991;

        Pavri et al., 1992; Glaze, 2008).

Pit Chains: a string of circular to elliptical pit craters (<1 – 10 km diameter) interpreted

        as the product of subsurface stoping of material during magmatic dike

        emplacement (Okubu and Martel, 1998).

Radial structures: structural lineaments radiating from a common center [Fig. 8].

Shield: <10 km circular features with domes, cone, or flat top shapes. They are

        interpreted as small volcanic edifices (Guest et al., 1992).

Wrinkle Ridges: sinuous ridges (Stofan et al., 1993).

Results and Analysis

The global survey resulted in identification of 55 circular lows. All measurements and characteristics are recorded in Plate 1 (on compact disk). The circular lows show no preference of geographic location on the planet. Circular lows range in diameter from 69 to 441 km, with a mean diameter of 163 km. Ellipticity ranges from 0.66 to 1, with mean ellipticity of 0.90. Depth ranges from 0.10 to 2.55 km (mean of 0.70 km). All but four circular lows display rims, with rim heights ranging from 0.10 to 1.60 km, mean rim height of 0.50 km. The spatial settings of circular lows are unlike those of coronae; 91% of circular lows occur as isolated features whereas only 10% of coronae occur as isolated features; 65% of all coronae lie within chains, whereas only 9% of circular lows lie within chains. Topographically, circular lows occur mostly within the lowland regions, although they do not occur within the deepest lowlands. By comparison ~10% of coronae lie within the lowlands. Approximately 70% of circular lows lie in close proximity to ancient ribbon-tessera terrain. All circular lows display annuli that range in structure type from folds, fractures, or both. The widths of concentric annuli around circular lows range from 5 to 160 km (mean width of 38 km); and annuli occur along the circular low edges in most cases. In most cases, concentric structures spread at least 108° around the circular low. Notably, only six circular lows display radial structures, unlike coronae which commonly display radial structures. The radial structures of all circular lows range in type from folds to fractures, which spread 90° to 360° around individual circular lows. Radial structures appear either in the interior or exterior of the six circular lows, showing no preference in location. Two circular lows display radial structures that extend on to the surrounding terrain. Only 13 circular lows

31

display lobate flows associated with the individual circular low, with areas of flows extending as much as 22 times the area of circular lows. Roughness of circular low basin interiors varies from smooth to rough. Many circular basins display shields with evidence of minor flooding. Features within the basin interiors include wrinkle ridges, fractures, impact craters, and pit chains. Steep-sided pancake domes are spatially associated with 17 circular lows, typically occurring within the interior and along the edges of circular lows, and rarely on the surrounding surface outside the circular low.

Circular lows are distributed across Venus, with 24 in the northern hemisphere and 29 in the southern hemisphere. Similarly, circular lows occur across both the eastern and western hemispheres. This suggests circular lows have no preferred location.

The diameter histogram [Fig. 9a] shows a range in diameter for circular lows from 69 to 441 km. The average size is 163 km and median is ~147 km. Most circular lows range in diameter from 69 to 252 km, an average of 150 km and median of ~141 km. Three circular lows, Rananeida Corona (Ra) in Metis Regio (V-6), Umay-ene Corona (Ue) in Agnesi (V-45), and Aramaiti Corona (Ar) in Aino Planitia (V-46) have diameters greater than 300 km. Apart from having large diameters, these three circular lows do not vary greatly in other characteristics compared to the rest of the circular low dataset and are therefore included in characterizing circular lows.

Most circular lows have ellipticity values ranging from 0.72 to 1 (average of 0.90, median of 0.92), satisfying the condition that selected features be circular [Fig. 9b]. An exception to this is Omeciuatl Corona (Om) in Niobe Planitia (V-23). Omeciuatl Corona has an ellipticity of 0.66; however, its close spatial proximity to circular low Bhumiya Corona may be a reason for its high ellipticity. The evolution of Bhumiya corona may

32
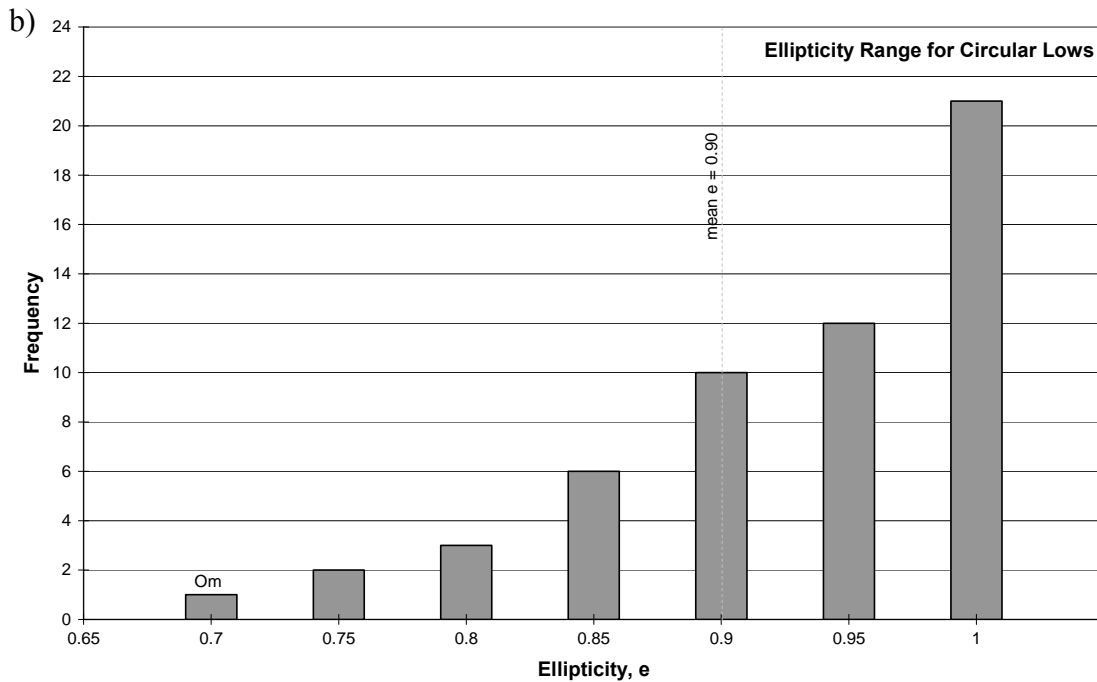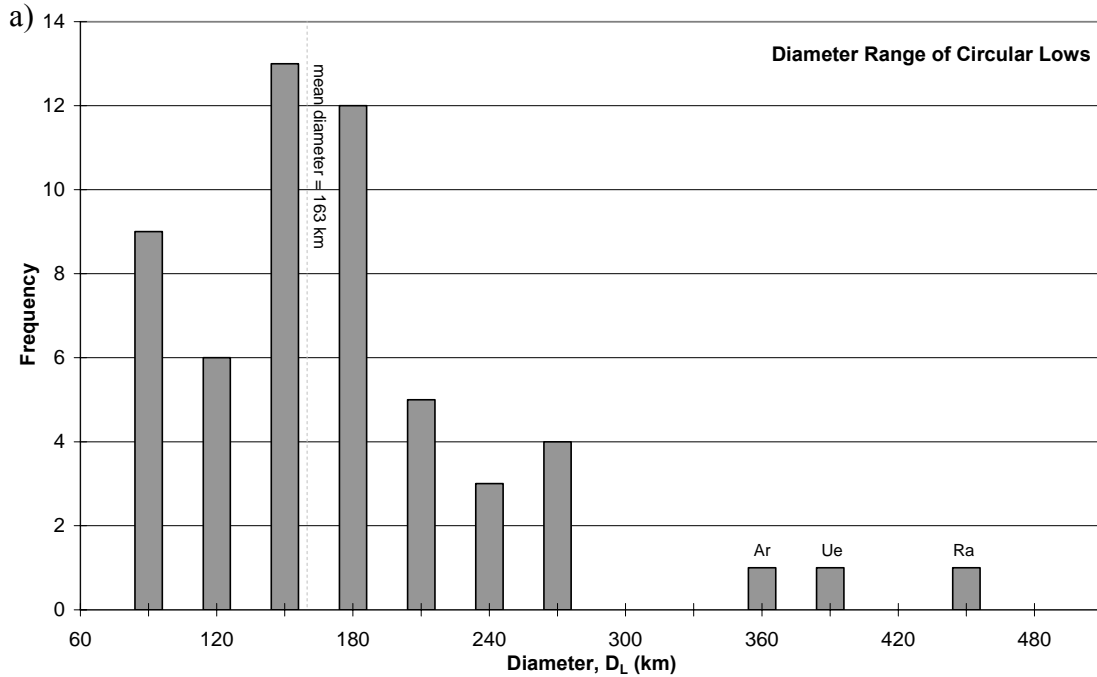
Figure 9. Characteristic frequency of diameter and ellipticity.
a) Circular lows vary in diameter between 69 to 441 km, an average size of 163 km, with the exception of Rananeida Corona, Ra (V-6), Umay-ene Corona, Ue (V-45) and Aramaiti Corona, Ar (V-46).
b) Circular lows are generally circular with a mean ellipticity of 0.90, with the exception of Omeciuatl Corona, Om (V-23).

have played a role in shaping Omeciuatl corona.

Basins of circular lows have depths ranging from 0.10 to 2.55 km, with a mean depth of 0.70 km and median of 0.50 km [Fig. 10a]. However most circular lows range in depth from 0.10 to 1.40 km, with a mean depth of 0.57 km and median of 0.50 km. Circular lows with depths less than 0.40 km are treated with caution due to poor GTDR resolutions. Increasing distance of the feature from the nearest edges of altimeter footprints can distort the measurements and small elevation variations may not be discernable. Circular lows in Lakshmi Planum (V-7), Hestia Rupes (V-22), and Taussig (V-39) quadrangles display the deepest basins [Fig. 10a]. The circular basins in these regions are not spatially close to each other. It is interesting to note that none of the "big" circular lows [Fig. 9a] are deep. In Lakshmi Planum quadrangle (V-7), the unnamed circular low, Un1 (74.5^{o}N, 314.5^{o}E), lies adjacent to Lakshmi Planum that extends across much of the quadrangle. It may be that the circular low is a byproduct of the much larger plateau-like generation of Lakshmi Planum. Detailed geologic mapping of this region is necessary to interpret if this is the case. It is also possible that the depth measurement is an artifact of the data collection method due to the coarse altimetry resolution. Collete Patera and Sacajawea Patera lie within Lakshmi planum and are interpreted from detailed geologic mapping and analysis to have deep interiors due to passive drainage from a non-replenished magma chamber (Roberts and Head, 1990). Ledoux Patera in Taussig (V-39) has a basin depth greater than 1.50 km and has therefore been identified as an outlier. Unlike the other circular lows with deep basins that lie within the highlands, Ledoux lies in the mesoland, spatially adjacent to a chain of coronae. It is possible that Ledoux
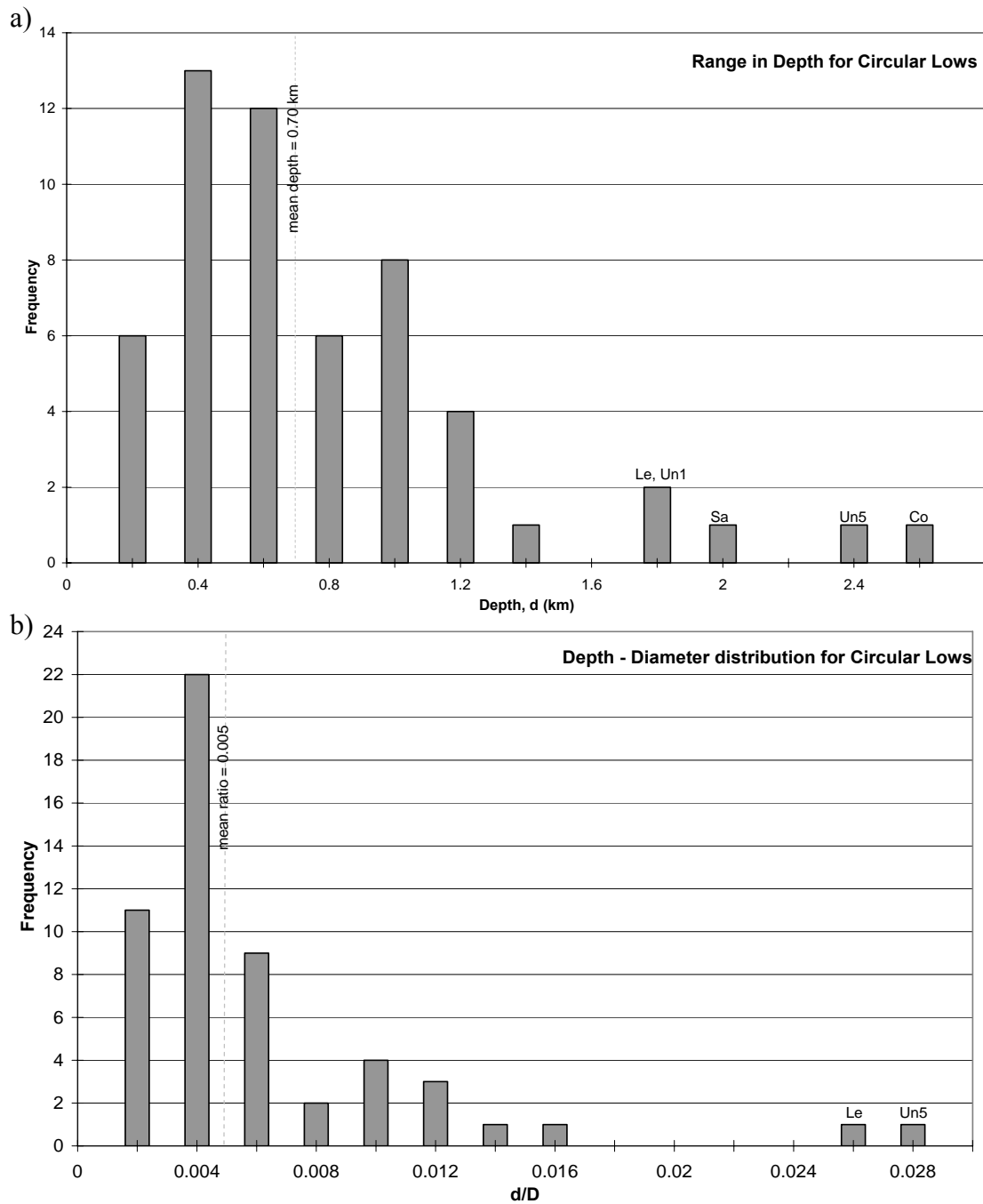
Figure 10. Characteristic frequency of depth and the aspect ratio.

a) Circular low interior depths range from 0.10 to 2.55 km, with a mean depth of 0.57 km. Five circular lows have depths greater than 1.50 km including unnamed circular lows in V-7 and V-22 (Un1 at 74.5°N, 314.5°E and Un5 at 1.5°N, 72°E respectively); Collete Patera (Co) and Sacajawea Patera (Sa) in V-7; and Ledoux Patera (Le) in V-39.

b) The depth-diameter aspect ratio of circular lows show a strong maximum at 0.004. The unnamed circular low in V-22 (Un5) and Ledoux Patera (Le) in V-39 are treated as outliers.

Patera formed the same way as the coronae chains. Along with a deep basin, Ledoux Patera has a diameter of 72 km (and therefore could be suspect) and also displays lobate flows that cover 22 times the area of the circular low, another characteristic typical of coronae and atypical of circular lows. The unnamed circular low in Hestia Rupes (V-22), Un4 (1.5°N, 72°E; diameter 85 km), has the second deepest basin of all circular lows (2.30 km), which may either be an artifact measurement, due to its small diameter, or the end product of a unique process.

Depths of the circular lows are normalized to basin diameters representing the slope of circular lows [Fig. 10b]. This distribution of d/D values shows that most of the circular low group has similar depth-diameter aspect ratio, with an average value of 0.005 and median value of ~0.004. Two circular lows are outliers with respect to aspect ratio, suggesting that either these circular lows are extremely deep or the circular lows are anomalously small. The unnamed circular low (Un5) in Hestia Rupia at 1.5°N, 72°E (V-22) and Ledoux Patera (V-39) are outliers with respect to the slope as expected due to their deep interiors. Both are also very small features. However the big circular lows have depths such that their ratios fall into the general ratio range.

Fifty one circular lows are enclosed by rims. Rims vary in height from 0.10 to 1.60 km, with a mean rim height of 0.5 km and median height of 0.45 km [Fig. 11a]. In most cases, the rim heights range from 0.10 to 1.40 km (mean height 0.48 km, median height 0.43 km). Rim height is not uniform around the individual circular low in most cases, and most rims do not completely surround the circular low. This is either
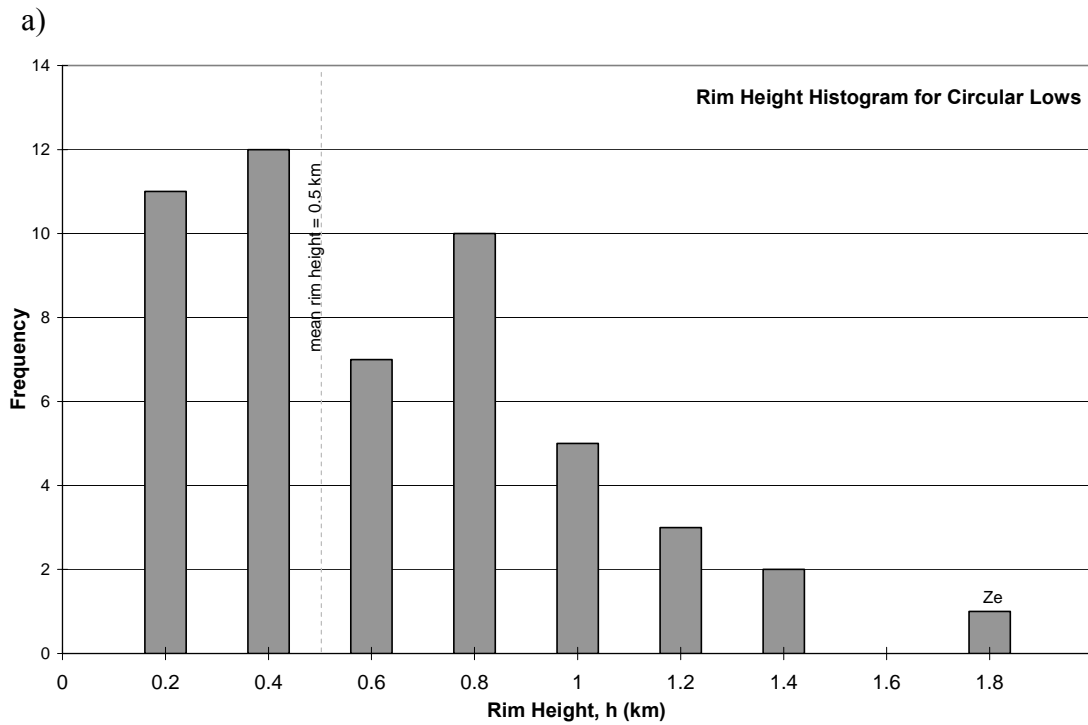
a)

Figure 11. Characteristic frequency of rim heights present in 51 circular lows.
    a) This indicates rims are present around 51 circular lows. Rim heights range from
          0.1 km to 1.6 km, with a mean height of 0.5 km. Zemaite Patera (Ze) in V-52
          has a rim height of 1.6 km, and is treated as an outlier.

indicative of formation processes or indicates post-formational modification. In some cases, annuli structures coincide with the rims. Only one circular low, Zemaite Patera in Helen Planitia (V-52) located within the highland, has a rim height of 1.6 km although the depth-diameter aspect ratio falls in the general range with other circular lows. The frequency of rim height normalized to diameter of circular lows is summarized in Figure 11b. In general the ratio ranges from 0.001 to 0.023, with a mean ratio of 0.003 and median ratio of 0.002. For most circular lows the ratio ranges from 0.001 to 0.011, with a mean ratio of 0.003 and median ratio of 0.0025. The distribution shows a strong maximum for a ratio of 0.004. Ledoux Patera in V-39 and Zemaite Patera in V-52 have the greatest ratio and are considered outliers. Zemaite Patera has a great rim height (Fig. 11a) and a very small diameter, therefore justifying it as an outlier with respect to diameter. Ledoux Patera is as an outlier due to its small diameter relative to its rim height.

The frequency of rim height normalized to depth of circular lows is summarized in Figure 11c. In general the ratio ranges from 0.1 to 8, with a mean ratio of 1.2 and median ratio of 0.85. For most circular lows the ratio ranges from 0.11 to 6, with a mean ratio of 1.1 and median ratio of 0.8. The distribution shows a strong maximum for a ratio of close to 1 suggesting that rim heights are the same heights as the depth of circular lows. Only Omeciuatl Corona in V-16 has the greatest rim height to depth ratio, a value of 8, which is expected as it is very shallow and has rim height of 100 m. Omeciuatl is interestingly elliptical in shape.

Four circular lows do not display rims; although these features have diameters, and structural characteristics (including a lack of radial flows) similar to other circular
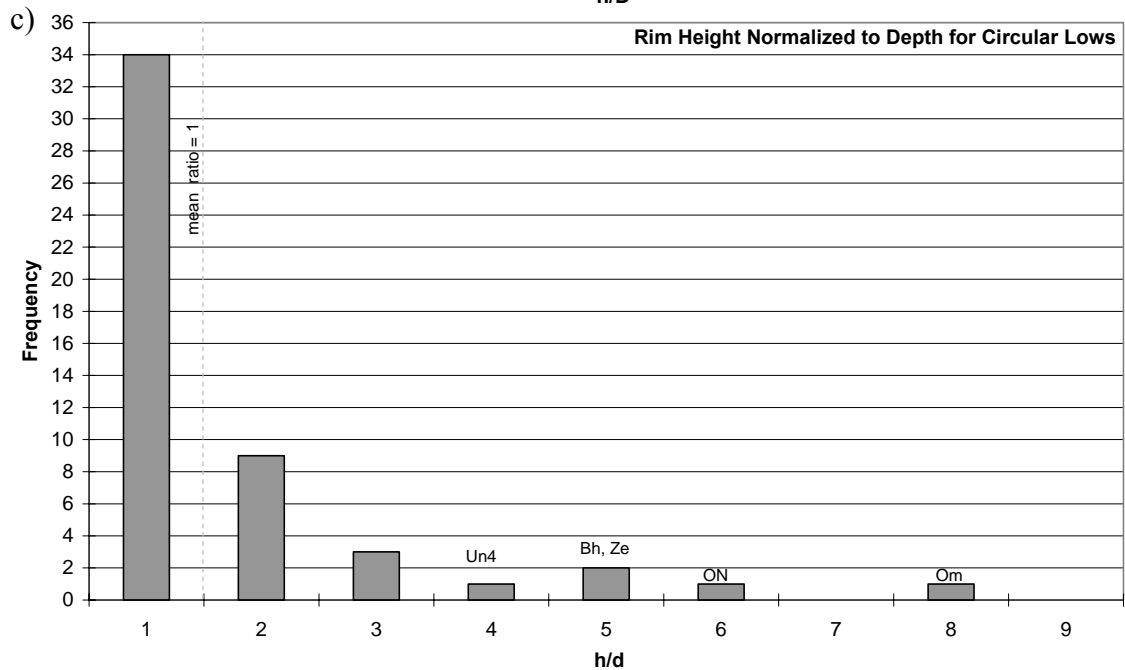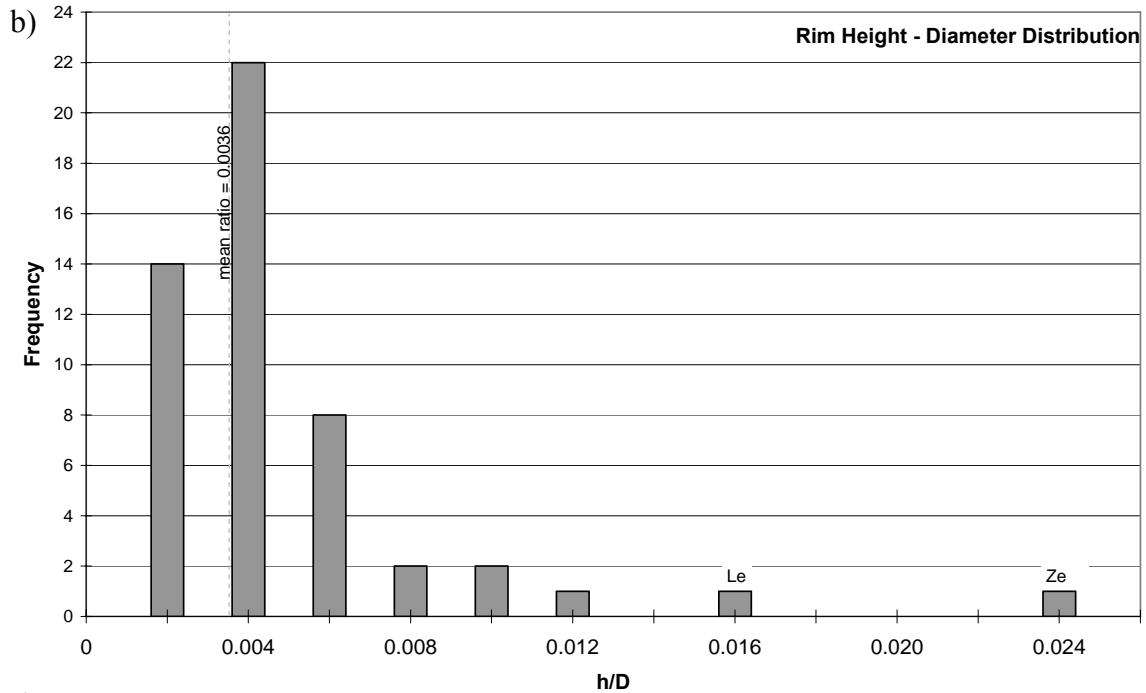
Figure 11. Characteristic frequencies of rim heights normalized to the diameter and depths for circular lows.
b) Rim heights normalized to the diameter of circular lows is strong at a ratio of 0.0036. However, Ledoux Patera (Le) in V-39 and Zemaite Patera (Ze) in V-52 have a large ratio and are treated as outliers.
c) Majority of circular lows show a 1:1 relation between the rim height and basin depth. Omeciuatl corona (Om) and Bhumiya Corona (Bh) both in V-23; Obasi-Nsi Corona (ON) in V-60; Zemaite Patera (Ze); and the unnamed circular low (Un4) are outliers.

lows. Only one circular low, Qakma Corona in Ganiki Planitia (V-14), displays radial fractures extending into the surrounding terrain but lacks a rim.

Topographically, circular lows occur in the lowland (45%) and mesoland (43%) regions of Venus, with the remaining occurring in the highland (12%). Circular lows avoid the deepest lowland basins.

Spatially, circular lows occur mainly in isolated settings (91%) and rarely in chains (9%); no clustered circular lows were recognized. This is significantly different from coronae. In the case of coronae, only 10% occur as isolated features, which lie in the lowlands.

At a global scale, spatial relations between circular low positions and tessera terrains were recorded using ArcGlobe[TM]. Ribbon-tessera terrain is characterized by ribbon structures (Hansen and Willis, 1996; Hansen and Willis, 1998). A circular low is considered adjacent to ribbon-tessera terrain if ribbon-tessera lies at least a diameter from the circular low edge. Approximately 60% of circular lows lie adjacent to tessera terrain. However, this does not lead to any particular conclusions about how circular lows form. It may be outside the resolution of SAR images to locate the tessera terrain completely without referring to high resolution images and moreover, cataloging the global distribution of tessera terrain is still ongoing.

Structurally, all 55 circular lows display well-defined concentric structures. The annuli structures range from troughs (fractures), to ridges (folds), and occasional pit chains. Many circular lows have ambiguous lineaments (30%) making it difficult to interpret possible stress relations associated with individual circular lows. Detailed geologic mapping of individual circular lows using high resolution SAR images is

a) Normalized Degree Spread of Concentric Structures

mean spread = 0.71 or 255°

Ro

$C_\theta°/360°$

b) Width of Concentric Structures for Circular Lows

mean width = 38 km

Un2   IL

Width, C_w (km)
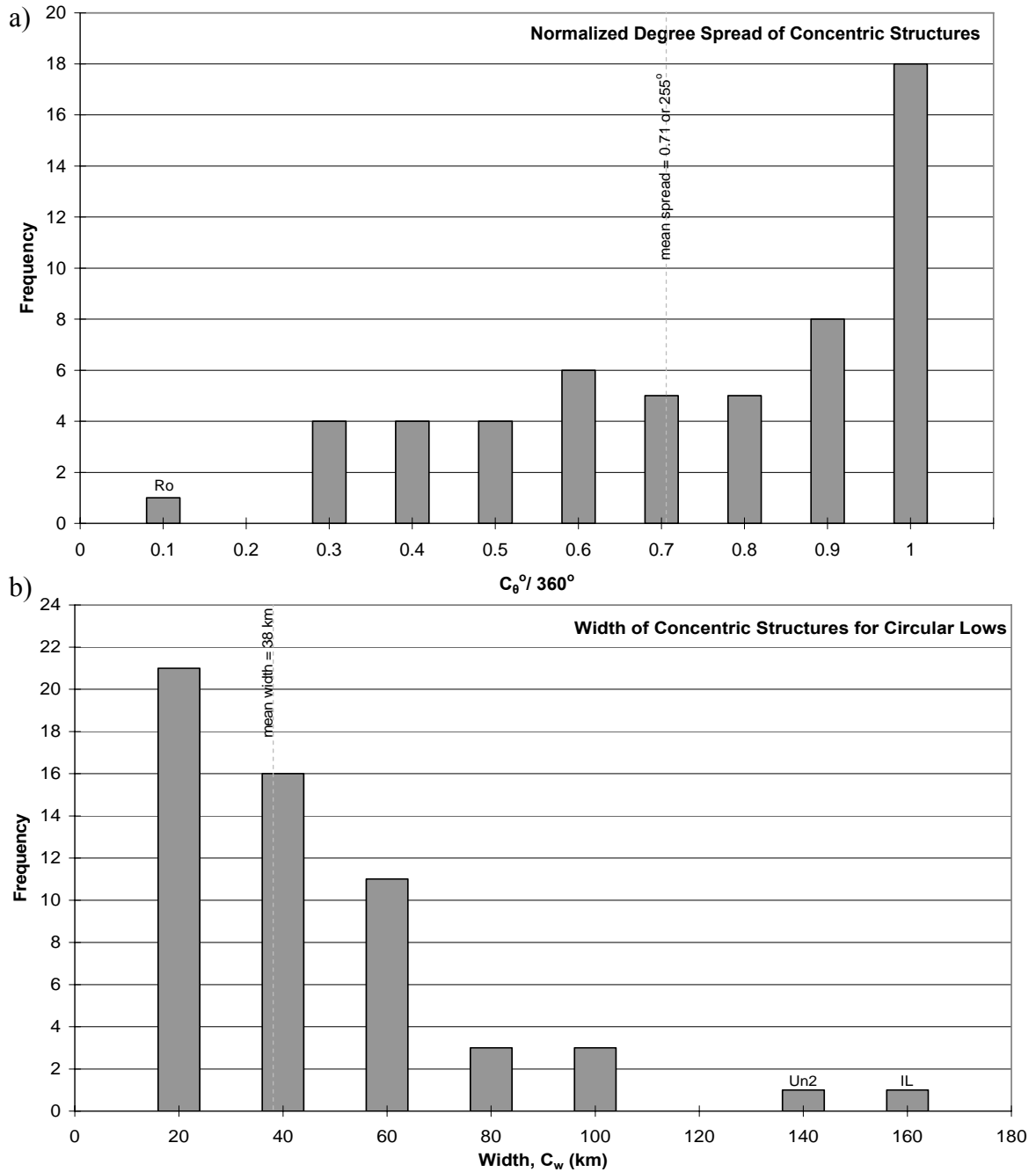
Figure 12. Characteristic frequencies of annuli structures including the degree spread and width.

a) Most circular lows display concentric structures spread completely around the feature, an average degree spread of 255°, with the exception of Rogneda Patera (Ro) in (V-39) surrounding < 40° of the circular low.

b) Annuli range in widths from 5 km to 160 km, an average of 38 km. An unnamed circular low (Un2) in V-16 and Ilyana Corona (IL) in V-57 have the widest set of annuli.

necessary to determine the character and cross-cutting relations of such structures. Annuli are generally distributed around the circular low with a mean spread of 255° and a median spread of 273° [Figs. 8, 12a]. Most circular lows display annuli surrounding between 83° and 360°, with a mean spread of 255° and median spread of 273°. A high frequency of circular lows display annuli completely around them. Only Rogneda Patera in Taussig quadrangle (V-39) has concentric structures surrounding ~35° of the feature. There are no lobate flows associated with the circular low to explain the lack of annuli around the feature, however it is spatially close to a coronae chain and lobate flows from the chain may have buried part of the annuli which can be confirmed through detailed geologic mapping of the area.

The frequency of total widths of concentric structures around circular lows is summarized in Figure 12b. Total widths range from 5 km to 160 km, with mean and median widths of 38 km and 30 km respectively. In most cases, the widths range from 5 km to 100 km, with a mean width of 34 km and median width of 30 km, and a strong maximum at 20 km. An unnamed circular low (Un2, 31.5^{o}N/255.5^{o}E) in Kawelu Planitia (V-16) and Ilyana Corona (IE) in Fredegonde (V-57) have the largest widths of annuli at 125 km and 160 km respectively.

The widths of annuli are normalized to the radii of circular lows in order to determine the thickness of annuli relative to circular lows [Fig. 12c]. Ratios less than one indicate narrow bands and wide bands for ratios greater than one. Ratios equal to one would indicate that the annuli are as wide as the radius of circular lows. The annuli in general appear closely spaced to each other. Ratios range from 0.11 to 1.67 with a mean and median ratio of ~0.50 and 0.37 respectively. Most circular lows have thickness ratios
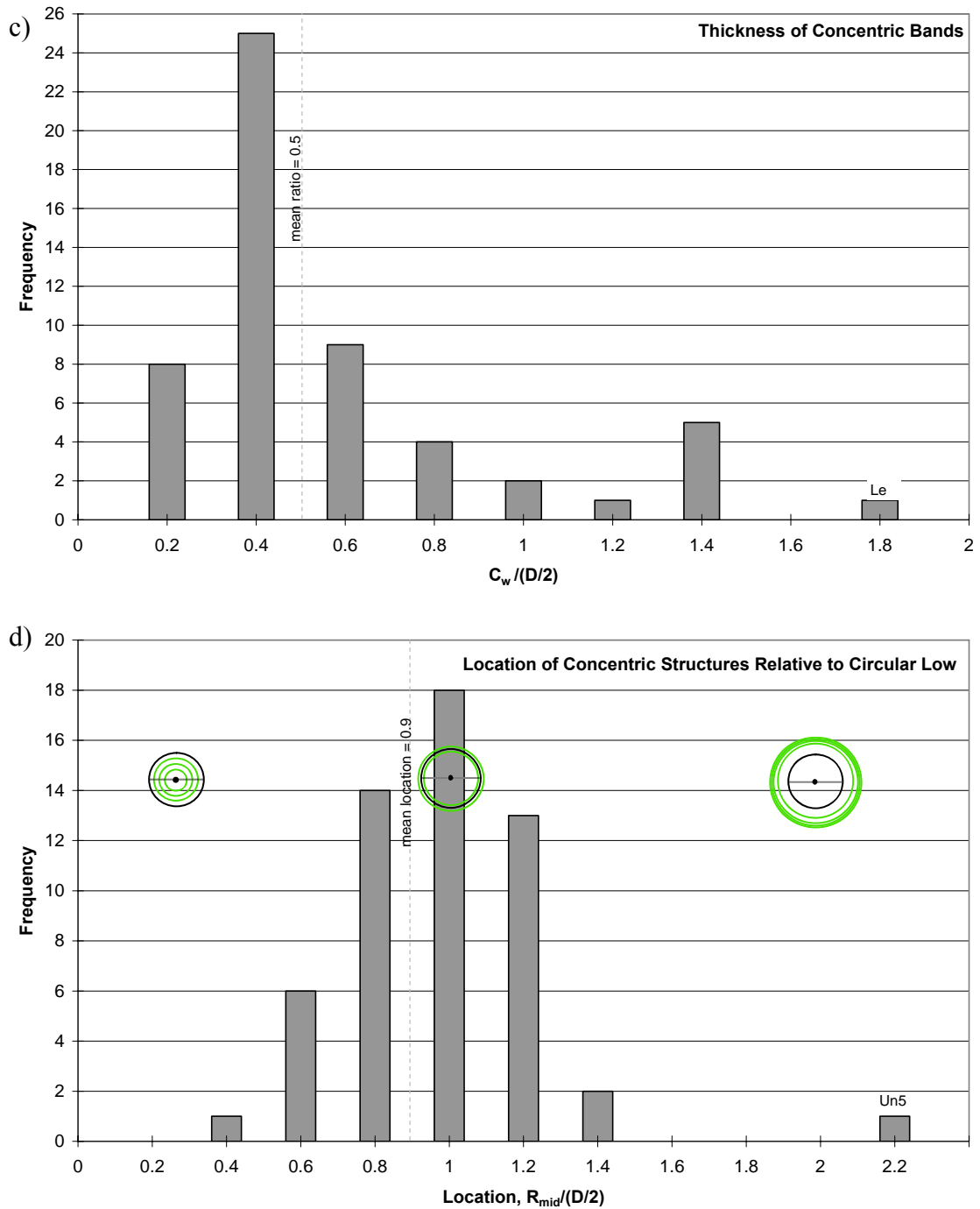
Figure 12. Characteristic frequencies of annuli structures including the thickness and the location of concentric structures.

c) Annuli thickness is determined by normalizing the annuli width to radii of circular lows. Most circular lows have thin or narrow annuli (thickness ratio < 1), with the exception of Ledoux Patera (Le) in V-39.

d) Location of annuli is determined by normalizing the midpoint of annuli width to radii of circular lows. A majority of the annuli are located along the edges of circular lows (ratio = 1) with the exception of an unnamed circular low (Un5) in V-39.

43

ranging from 0.11 to 1.39, a mean and median ratio of 0.47 and 0.36 respectively. The

strong maximum at 0.40 indicates most circular lows have narrow bands of concentric

structures. The narrow bands around circular lows suggest the annuli formed on a thin

lithosphere because the spacing reflects the layer thickness. On a thick lithosphere, the

structures would not be visible. Detailed geologic mapping of high-resolution images of

the circular lows can better indicate the true spacing of individual annuli bands. Only

Ledoux Patera (V-39) represents an outlier with regard to annuli thickness.

The locations of concentric structures relative to circular lows might provide clues

to circular low formation. I normalize the midpoint of concentric structure widths (R_{mid},

[Fig. 8]) to the radius of the individual circular low. Generally, ratios less than 1 indicate

that the annulus lies within the circular low interior. A ratio of 1 indicates that the

annulus lies along the topographic edge with a part of the annulus within the interior and

extending out into the surrounding area. Ratios greater than 1 indicate that the entire

annulus lies outside the circular low basin. Figure 12d summarizes the location of

concentric structures relative to circular lows. In general circular lows show a near quasi

normal distribution with annuli present within the basin interior, along the edges, and on

the exterior, with a mean and median ratio of 0.88 and 0.89 respectively. Most circular

lows lie within the interior and along the feature edges. There is only one circular low,

an unnamed feature (Un5, 22°S/214°E) in Taussig quadrangle (V-39) that acts as an

outlier with the annulus completely outside the edges and onto the surrounding terrain.

Relation between the thickness and location of concentric structures relative to circular

lows indicates a majority of circular lows (76%) display narrow annuli that lie within the

basin interior or along the edges [Fig. 12e]. The outliers include Ledoux Patera (Le) with

e)
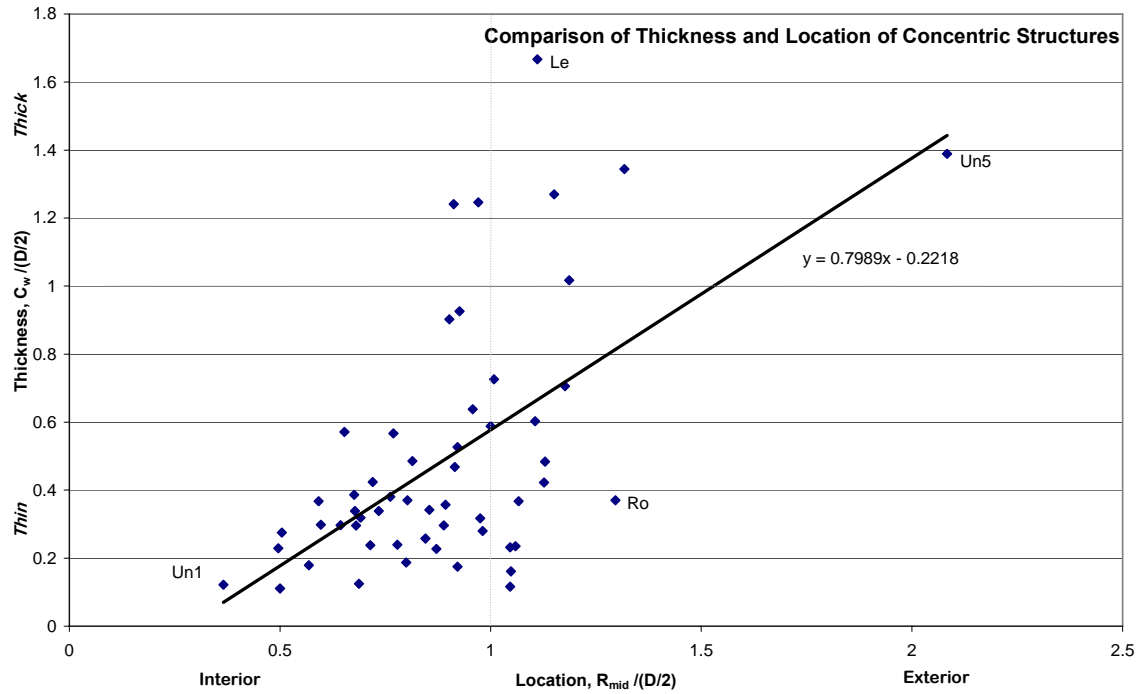
Figure 12. A plot of location and thickness of concentric structures for circular lows.
e) Concentric structures surrounding most circular lows appear thin and within the basin interior, with the unnamed circular low (Un1) in V-7 displaying very thin annuli. Outliers included Ledoux Patera (Le), Rogneda Patera (Ro), and an unnamed circular low (Un5) at 22°S, 214°E all within the same quadrangle, Taussig (V-39) and displaying annuli that are thick and located in the exterior.

thick bands (ratio ~1.7 times the radius) and located just outside the feature edge, Rogneda Patera (Ro) with thin bands (ratio ~0.3 times the radius) yet located out in the surrounding, and an unnamed circular low (Un5) at 22°S, 214°E with both thick bands and located at the exterior. Interestingly, these outliers all are located within the same quadrangle, Taussig (V-39). Two of the three outliers, Rogneda Patera and Ledoux Patera are spatially associated with coronae chains, a possible product of chain generation of coronae (however this is too small a circular low count to conclude if such is the case). The unnamed circular low in V-7 is also an outlier in a different sense; it has the narrowest annulus band, located close to the basin centre.

Only six circular lows display radial structures [Fig. 13a]. The radial structures in all but one case are fractures. Qakma Corona in Ganiki Planitia (V-14) displays ridges. All but one of these circular low lie within the northern hemisphere, located mainly in the lowland; one lies in the mesoland. Circular lows with radial structures range in diameter from 117 to 247 km, with a mean diameter of 167 km. Ellipticity of basins with radial fractures range from ~0.80 to 1, with a mean ellipticity of 0.91. The depths of circular lows with radial signatures range from 0.15 km to 1.40 km, with a mean depth of 0.92 km. These circular lows, like almost all circular lows, are spatially isolated. Three of the six circular lows have spatially associated lobate flows.

The foci of radial structures in most circular lows are not visible. However, extrapolating the radial structures leads to a common origin within the interior of each circular low. A more important observation is that only two circular lows, Qakma Corona in Ganiki Planitia (V-14) and Nalwanga Corona in Kawelu Planitia (V-16) display radial structures extending out onto the surrounding terrain. The remaining four

a)
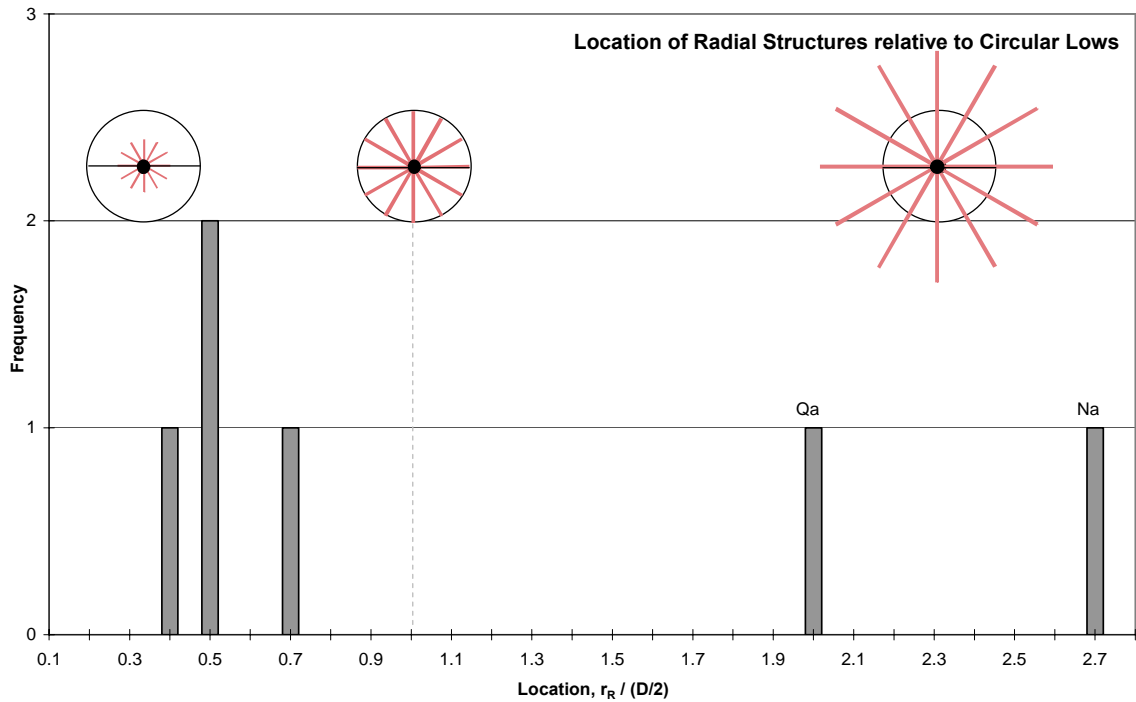
Figure 13. Frequency plot of circular lows displaying radial characteristics.
a) Location of radial structures is determined by extent of radial structures to radii of
circular lows. Of the six circular lows with radial structures, four display structures
that lie within the basin interior (location ratio < 1). Qakma Corona (Qa) in V-14 and
Nalwanga Corona (Na) in V-16 display display radial structures extending well into
the exterior surroundings.

circular lows display radial fractures completely within the interior basin that extend 0.30 to 0.68 times the radius of the circular low. None of these four circular lows displays any obvious lobate flows associated with radial fractures. Therefore the lack of fractures along or beyond the basin edge is not likely due to burial. The lack of lobate flows suggests that the radial fractures occur more locally within the basin interior, and perhaps post-dated, or formed late during the formation of individual circular lows. The remaining two circular lows show fractures that extend from the interior outward, up to 2.6 times the radii.

Qakma Corona in Ganiki Planitia (V-14) displays radial fractures ridges with the exterior extending onto the surrounding surface by a distance of two radii, indicating that the fractures formed during the formation of Qakma Corona [Fig. 13b]. The largest circular low with radial fractures, Nalwanga Corona in Kawelu Planitia (V-16), displays both radial fractures, and a narrow lobate flow [Fig. 13c]. Detailed geologic mapping of Nalwanga Corona indicates a complex interior that records a complex history (J. Jacobs, unpublished mapping and personal communication, 2008).

Shields and radar-smooth material occur across much of the surface of Venus (Guest et al., 1992). However, only 13 circular lows (24%) display associated lobate flows [Fig 14]. This indicates that there is no strong correlation between lobate flows and circular lows. In order to determine spatial correlation between lobate flows and circular lows, I compared the areas of both lobate flows and circular lows (A_{flow}/A_{CL}), and the depth-diameter aspect ratio for circular lows (d/D) [Fig. 14]. Seven circular lows show a less than 1:1 relation between the areas and depth-diameter aspect ratio. These relationships indicate that the lobate flows are more localized around such circular lows.

b)
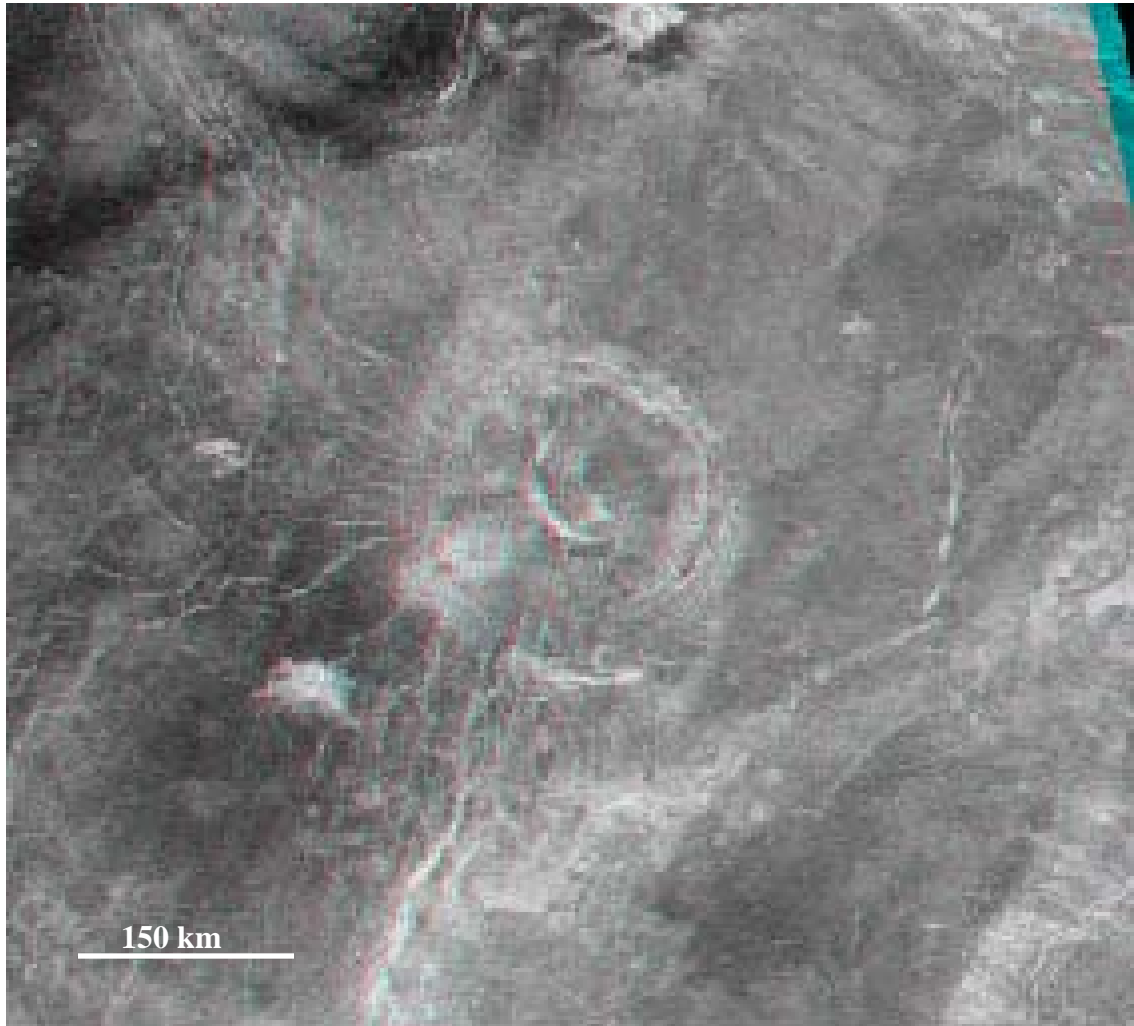
Figure 13. SAR image of circular lows displaying radial structures that extend out to the
surrounding terrain.
b) Qakma Corona, an isolated circular low located in lowlands of Ganiki Planitia
(V-14), 35.5°N, 207°E, displays radial structures (ridges) extending out a
distance two times the feature radius of 68 km.

c)
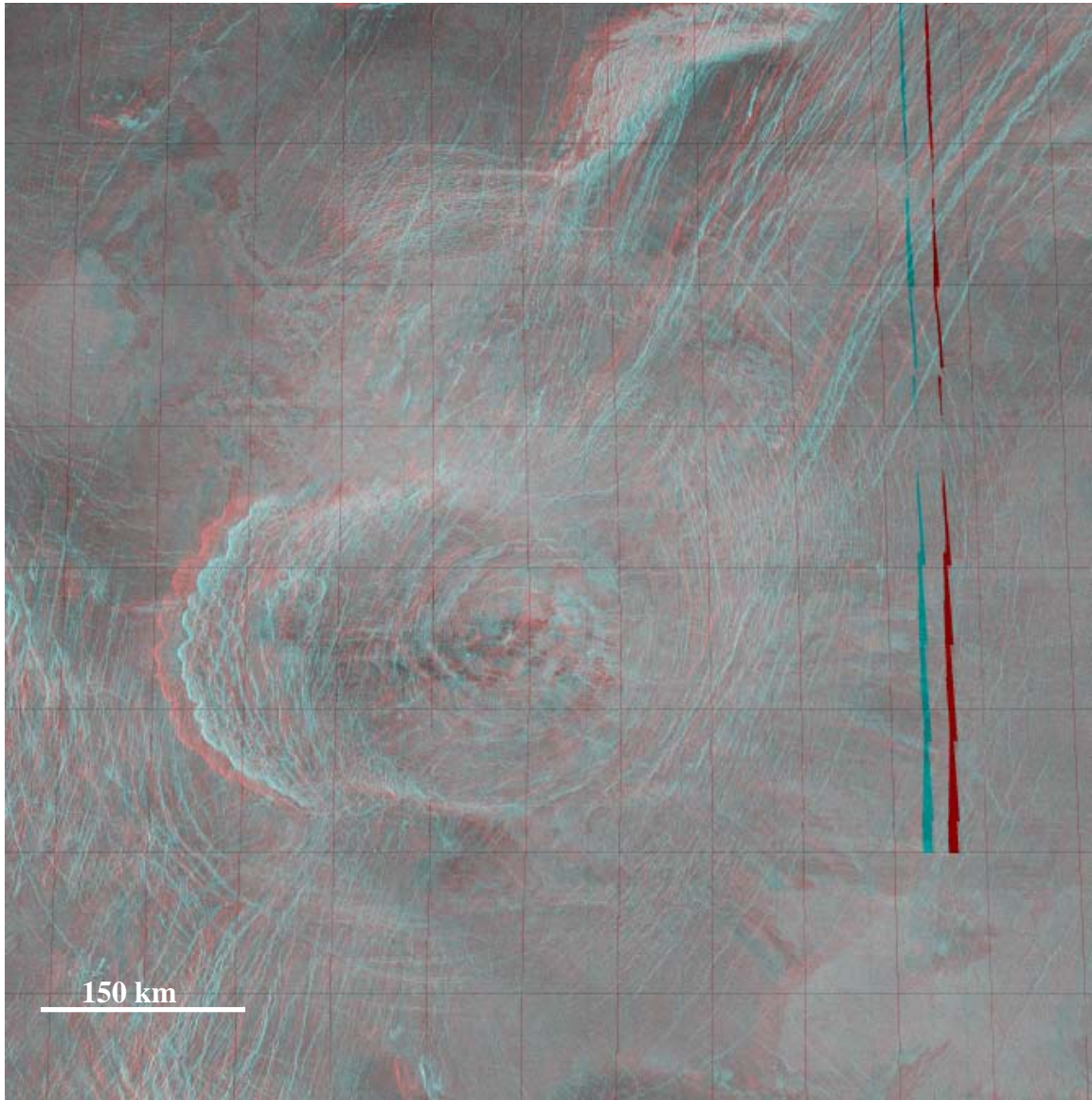
Figure 13.
      c) Nalwanga Corona, another isolated circular low located in lowlands of Kawelu Planitia (V-16), 48.5°N, 246°E, displays radial structures (ridges) extending out 2.6 times the feature radius of 69 km.
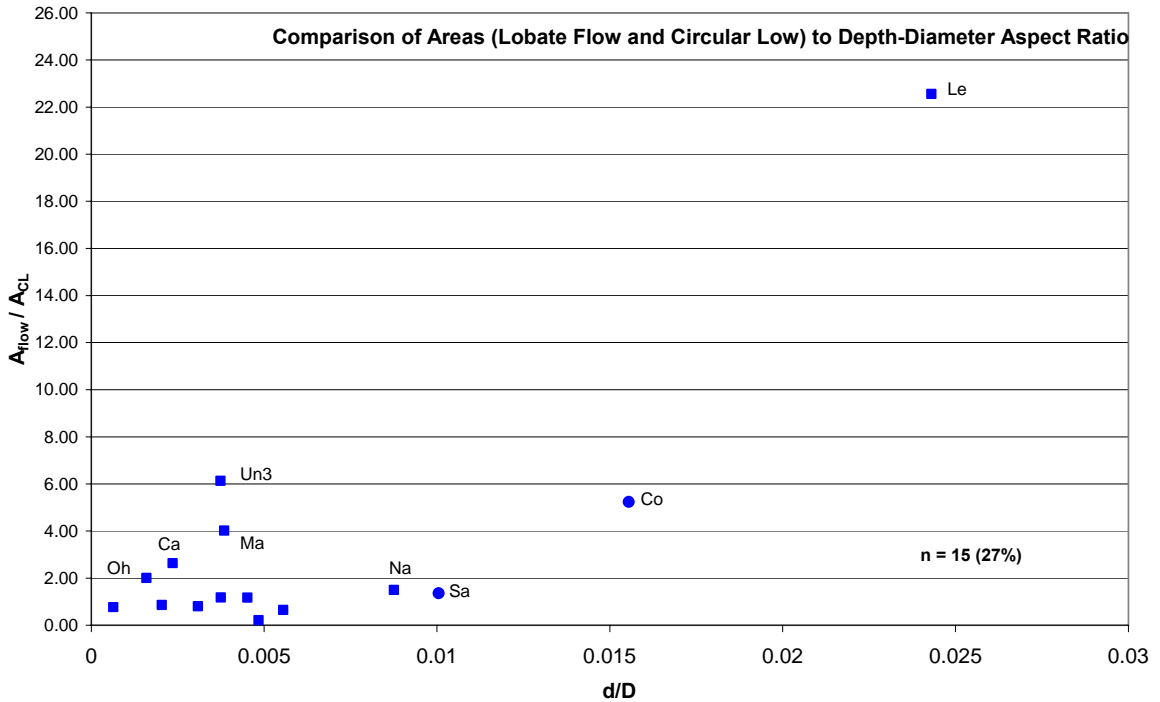
Figure 14. Coverage of lobate flows around circular lows compared to the depth-diameter aspect ratio. Typically, lobate flows associated with circular lows cover an area equal to that of the circular low. Outliers (where flows extend greater than one circular low diameter) include Ledoux Patera (Le) in V-39; Nalwanga Corona (Na) in V-16, and an unnamed circular low at 27.8°N, 242°E (Un3) both in V-16; Ohogetsu Corona and Calleach Corona both in V-46; Collete Patera (Co) and Sacajawea Patera both in V-7; and Madderakka Corona (Ma) in V-30.

Other lobate-flow bearing circular lows vary between two to six times the aspect ratio including an unnamed circular low (Un3) in Kawelu Planitia (V-16), Madderakka Corona in Guinevere Planitia (V-30), Ohoghetsu Corona and Cailleach Corona both within Aino Planitia (V-46). These circular lows: lie within the lowland and mesoland parts of the planet, are circular features, range in diameters from 72 km and 247 km, and have shallow depths. They display no preference in topographic setting, or circular low characteristic to explain the large extent of lobate flows. In an extreme case, lobate flows extend outward covering as much as 22 times the area of the circular low (Ledoux Patera in V-39), however this circular low is exceptional and the close spatial setting of Ledoux Patera to coronae chain may attribute to the large extent of lobate flows. Only two circular lows, Nalwanga Corona in V-16 and Madderakka Corona in V-30, display both radial structures and lobate flows, characteristics common to coronae.

Circular low interior basins display a variety of characteristics, including: interior peaks, smooth surfaces peppered with shields, rough surfaces cut by fractures, wrinkle ridges, impact craters, and pit chains. A subset of 19 circular lows display peaks in their basin interior, although these peaks are not necessarily centrally located. The local and regional trends of structures such as fractures and wrinkle ridges are evident in and around circular lows. Detailed geologic mapping of individual circular lows is necessary to determine the emplacement history and structure timing.

Steep sided domes (generally < 10 km in diameter), also known as pancake domes, occur in spatial association with 16 circular lows. Pancake domes occur on the edges of eight circular lows, and in the exterior areas of eight circular lows. There is

debate within the Venus community as to how pancake domes develop; they are considered a class of volcanic features that form in response to variable magma viscosities (Head et al., 1991; Pavri et al., 1992; Glaze et al., 2008). Given that pancake domes are relatively rare across Venus (Pavri et al., 1992), their spatial association with circular lows might provide clues to pancake dome formation.

Implications

Coronae are quasi-circular features on Venus that occur in chains (60%), as clusters (30%), and isolated (10%). Coronae vary in topography from domes, to plateaus, and depressions. Many coronae preserve tectonic activity in the form of radial and concentric structures; and many preserve evidence of volcanic activity in the form of lobate flows. Type-1 coronae display complete or near complete annuli while type Type-2 coronae have less than 50 percent complete annuli. Type-2 coronae typically occur in the lowlands and have flat or depressed interiors (Stofan et al., 1992).

Circular lows are a morphological subset of coronae marked by amphitheatre-like depressions. Common characteristics of circular lows include: 1) a shallow depression (less than or equal to 1.5 km), 2) rims, 3) concentric annuli, 4) a lack of radial lineaments, and, 5) lack of geologic complexity in the immediate surrounding areas. Circular lows differ in a number of characteristics from coronae. Unlike coronae, circular lows generally occur as isolated features, and rarely occur in corona chains. Most circular lows lack radial fractures and radial lobate flows, which are common characteristics of coronae. Topographically, circular lows occur within the lowland, unlike coronae, which mostly lie in the mesoland. Very few circular lows display major flooding associated

with the formation of the circular low. Circular lows commonly display complete annuli yet occur in the lowland regions of the planet, making classification of circular lows as either Type-1 or Type-2 coronae difficult.

Based on the morphological classifications of coronae, ~165 coronae were predicted to classify as circular lows [Fig. 4]. However only 55 features, or 30%, have been classified as circular lows. Two assumptions I made in defining circular lows may explain for the small dataset, 1) requirement of circular plan-form, and 2) I only selected features that were free of geologic complexity in the surrounding terrain in order to avoid misinterpreting observed structures as product of any particular geologic process. Although circular lows are predominantly isolated features and only five are spatially close to coronae chains, this does not mean that circular lows are not among coronae chains. The assumption of selecting features free from complexity reduces the number of circular lows, and, in particular, those features located in chains or clusters.

Another observation is that circular lows dominate the lowland and mesoland regions of the planet but only ~10% lie in the highlands. The highlands typically comprise volcanic rises and crustal plateaus which are rich sources of volcanism. Possible flooding and burial of structures might explain the lack of features within the highlands.

Hypotheses

Different mechanisms have been proposed to explain the wide range of topographic and structural characteristics of coronae. The most common hypotheses of coronae formation are: 1) diapirs rising within the upper crust; 2) bolide impact craters; and 3) calderas (Stofan et al., 1991, 1992, 1997, 2001; Squyres et al., 1992; Janes et al., 1992; Smrekar and Stofan, 1997; Vita-Finzi et al., 2005; Hamilton, 2005; DeLaughter and Jurdy, 1997). These hypotheses considered with respect to the global database of 55 circular lows to determine which, if any, of the mechanisms best explain the observed characteristics of circular lows.

Diapir Hypothesis

The most widely accepted hypothesis for coronae formation involves the endogenic rise of buoyant mantle-derived diapirs to the base of the lithosphere and subsequent modification of the overlying surface resulting in corona formation (Stofan et al., 1991, 1992, 1997, 2001; Squyres et al., 1992; Janes et al., 1992; Smrekar and Stofan, 1997). Density contrast arises due to differences in temperature and composition, resulting in thermally or compositionally driven diapirs.

Topographic morphologies and structural responses that arise have been studied using experiments, dynamical calculations and finite-element models (Withjack and Scheiner, 1982; Cyr and Melosh, 1993; Koch and Manga, 1996; Stofan et al., 1991; Squyres et al., 1992; Janes et al., 1992). The experimental models involve circular doming under different conditions of local and regional stress fields. Models predict three stages of diapir evolution over which features and structures form [Fig. 15a]:

55
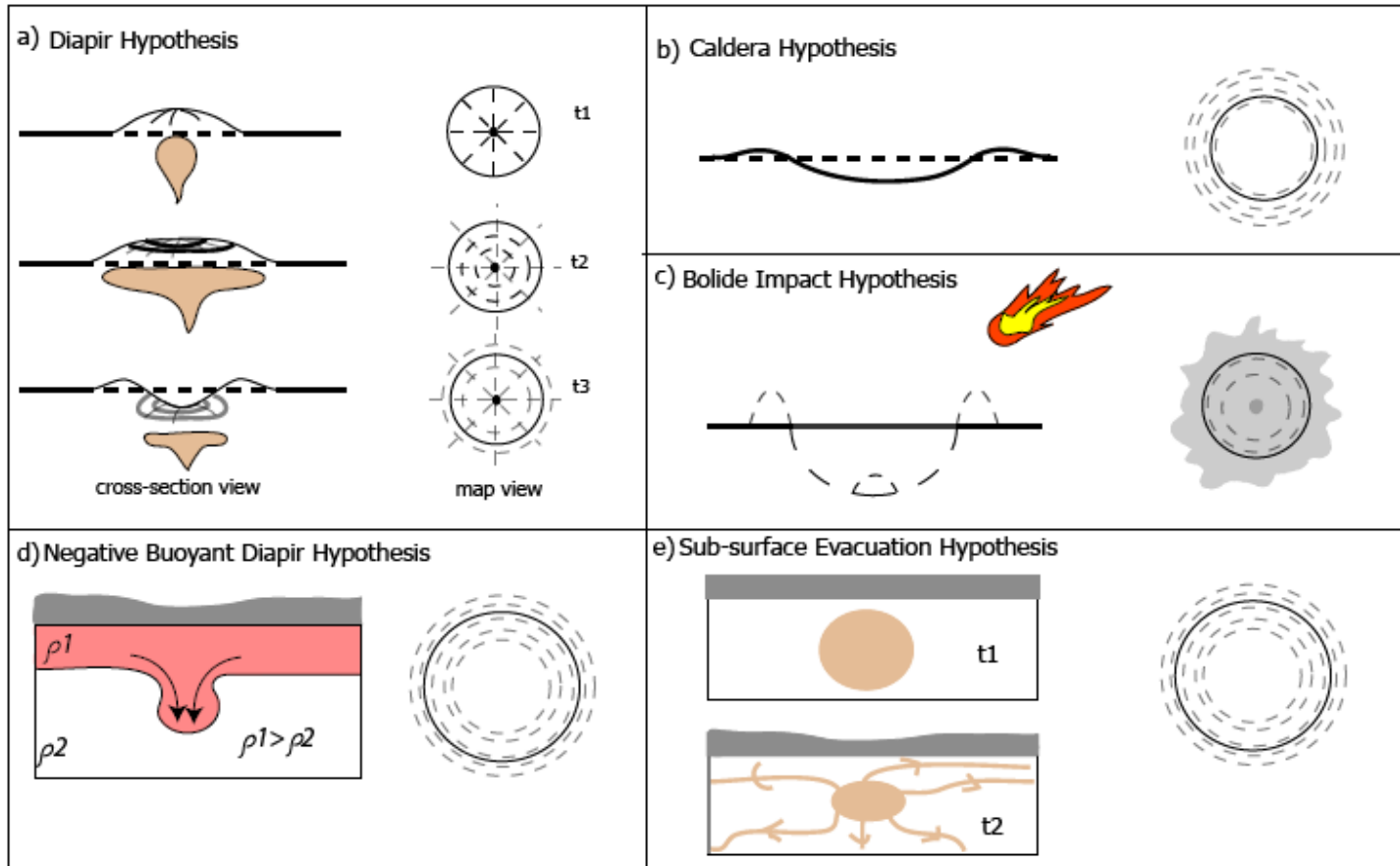
Figure 15. Cartoon illustrations of hypotheses to address the formation of circular lows.

a) Diapir hypothesis; t1) a rising buoyant mantle causes the overlying surface to dome up causing extension of fractures from the centre. t2) diapir spreads laterally creating a plateau-like feature and forming concentric fractures (Koch and Manga, 1996). t3) diapir cools causing a depression of the feature preserving all structures.

b) Caldera hypothesis; magma chamber collapse causes the surface to collapse forming rims and concentric fractures along the edges.

c) Bolide impact hypothesis; bolide strikes the surface causing interior excavation, ejecta, concentric rings, and possibly a central peak.

d) Negative buoyant diapir (subsidence) hypothesis; denser material sinks into the underlying layers causing a depression of the surface and generating concentric fractures along the edges.

e) Sub-surface evacuation (subsidence) hypothesis; drainage of pre-existing magma reservoir within the crust appears like a sinkhole on the surface with concentric structures over the area of drainage.

1) Rising diapirs uplift the surface to produce broad topographic domes with radial extension fractures. The scaling factor of the surface feature diameter is twice that of the original diapir (Whitehead and Luther, 1975). With active doming, faults commonly form across the uplifted surface. Both the outline shape of the dome and the presence of regional stress during doming affect the variety of fault patterns that appear (Withjack and Scheiner, 1982) [Fig. 16]. With an isotropic regional stress field, radial normal faults form initially along the edges of a circular dome. Experiments show that with increasing uplift, additional normal faults occur at the crests of the domes (Withjack and Scheiner, 1982; Cyr and Melosh, 1993). Normal faults are surrounded by an annulus of thrust faults. However, no deformation occurs at the external boundaries. In the presence of local differential stress fields and simultaneous doming, normal faults trend perpendicular to the regional extensional direction on the dome crests. With simultaneous doming and regional compression, normal faults form closely along the crest and trend parallel to the regional direction of compression. In the presence of local stress fields, radial structures are modified and can disappear entirely, and the general shape of the feature changes from circular to elliptical. With increasing differential regional stress, thrust faults evolve around the peripheries from full, to partial, and eventually disappearing altogether [Fig. 16]. The planform shape of the feature provides clues to the orientation of principle regional stresses, and as such can be used to interpret isotropic versus anisotropic regional stress fields due to feature formation.

At the second stage of diapir evolution, the diapir spreads laterally along the base of the lithosphere or at a neutrally buoyant layer (Stofan et al., 1992; Squyres et al., 1992; Janes et al., 1992; and Krassilnikov et al., 2001). Location of the neutrally buoyant level
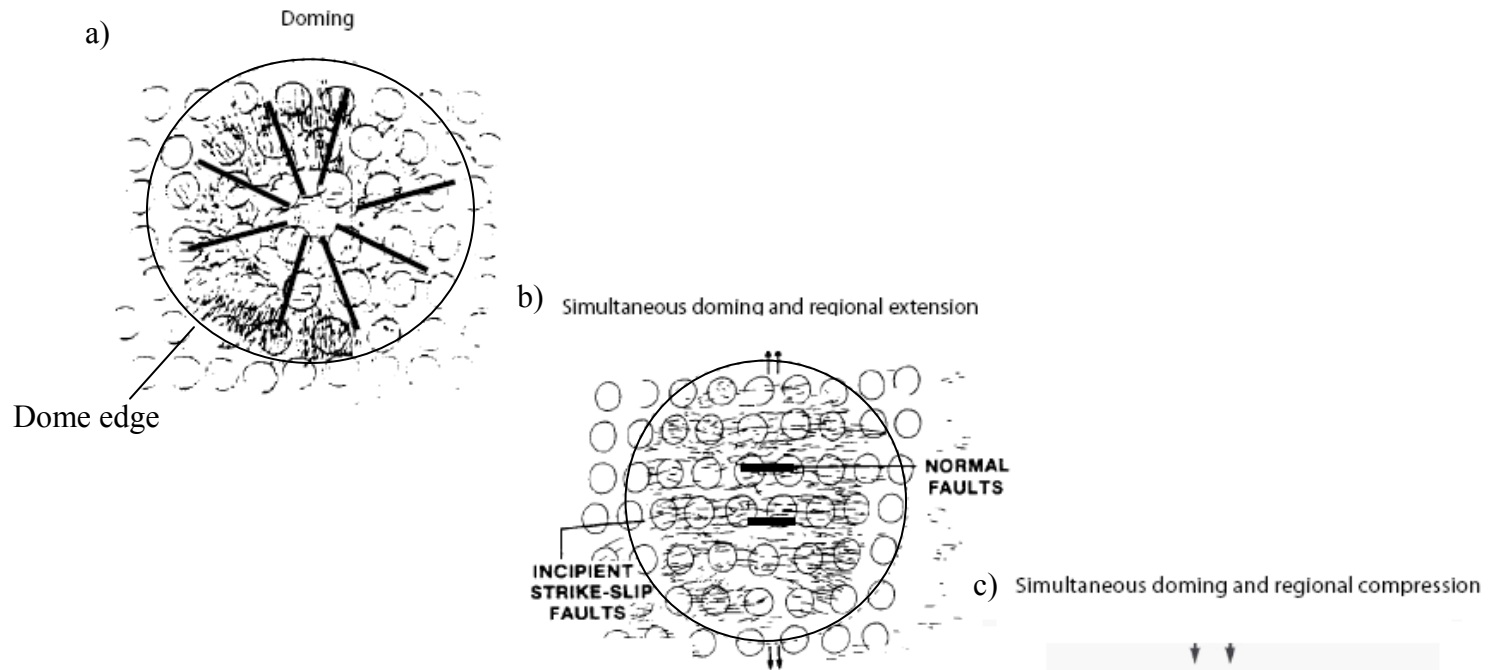
Figure 16. Surface responses to doming in the presence or regional stress (after Withjack and Scheiner, 1982).

a) With doming and no differential regional stress field, radial normal faults form, initially followed by additional normal faults along the dome edges with increasing uplift.

b) With doming and simultaneous regional extension, normal faults are decreasingly radial and eventually trend perpendicular to the direction of extension. The general shape of the feature changes from circular to elliptical, with the long axis parallel to regional extension. With increasing regional stress, thrust (strike-slip) faults evolve around the dome edges from full, to partial, and eventually disappearing altogether.

c) With simultaneous doming and regional compression, normal faults trend parallel to regional compression.
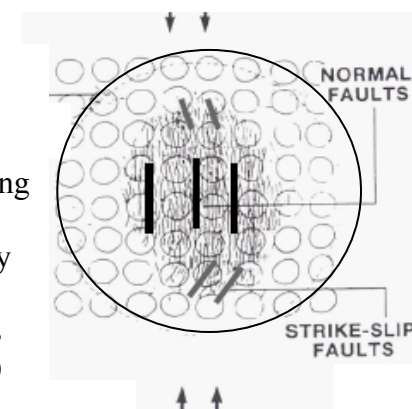
depends on the density of the diapir relative to the surrounding material, a function of both temperature and composition.

The ratio of the crustal thickness with the radius of the diapir determines the surface topography at this stage. For low ratios of crustal thickness and diapir radius, such as a ratio of 0.05 or less in the model by Koch and Manga, 1996; it is more typical for plateau- shaped topography to emerge. With increasing lateral spreading, the negative buoyancy due to the greater density of the diapir relative to surroundings is great enough to create a central depression. The position of the neutral buoyant layer determines how much surface deformation occurs from a laterally spreading diapir. For a layer deep within the crust, there is insufficient energy from the diapir to generate a plateau-shaped rise. At an intermediate position, a low topographic rise is possible. Koch and Manga (1996) modeled a 100 km diameter diapir (200 km diameter dome), and determined a dimensionless depth of neutral buoyancy, b/a, between 0.05 to 0.5 (where b is the thickness of the crust and a is the radius of the diapir, [Fig. 17]) in order for surface structures to form. With neutrally buoyant layers at shallow levels, there is sufficient energy in the diapir to spread laterally and result in a plateau-shaped rise. With greater lateral spreading, strike-slip faults along the concentric deformation become increasingly focused (Koch and Manga, 1996).

At the final stage, the cooling diapir loses thermal support, leading to the topographic relaxation of the uplift from the previous two stages. This relaxation results in a locally thickened crust (or lithosphere). A central depression forms above the relaxing model diapir and is more prominent when the overlying brittle layer is thin. Concentric rims and troughs form around the central depression. Concentric extensional
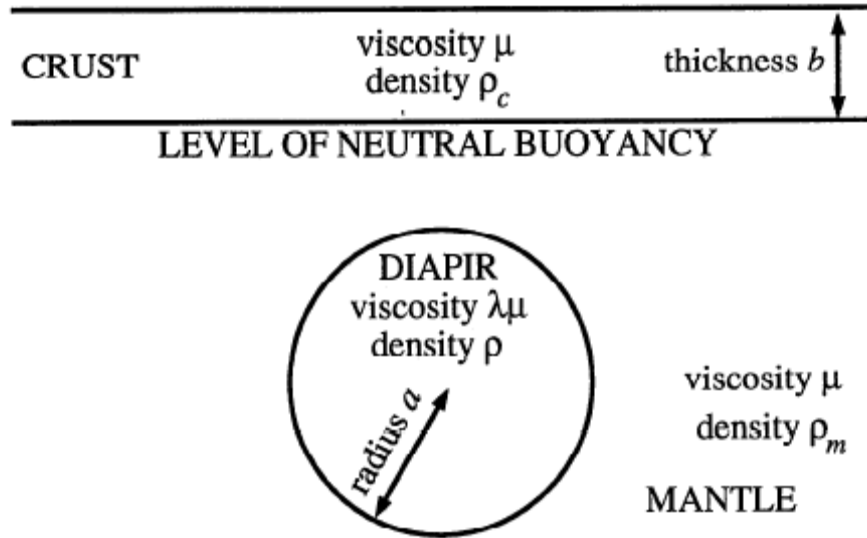
Figure 17. Model geometry of neutrally buoyant diapirs on Venus (after Koch and Manga, 1996). The diapir is at an initial depth of 10a.

fractures form inside and around the depression. Radial extension structures form in the central part of the structure and around the periphery; and radial compression structures appear on and beneath the slopes of the original plateau. The number and spacing of fractures produced decreases with increasing thickness of the overlying brittle layer superposing the model diapir. The second and third stages can partially coincide in time. Therefore the wide range of topographic, geomorphic, and geologic characteristics of coronae are interpreted as recording different stages of diapir evolution and not changes in lithospheres (Smrekar and Stofan, 1997).

Evaluation of Diapir Hypothesis

As diapirs rise through the crust, the overlying surface begins to deform, varying in morphology from domes, to plateaus, to circular depressions. Radial fractures are commonly associated with diapiric structures. Regional stress fields can alter radial fractures and in some cases completely dampen the development of radial structures. In the presence of local differential stress fields, fractures develop perpendicular to the minimum compressive stress (Withjack and Scheiner, 1982; Cyr and Melosh, 1993). But in such a case, the diapiric feature is no longer circular in planform, but takes on an elliptical shape.

Based on the diapir hypothesis, circular lows may form at the final stages of coronae evolution when the diapir cools and the overlying plateau relaxes to develop a depression in the central region surrounded by tectonic annuli. Circular lows range in diameter from approximately 70 to 440 km. A diapir producing such a feature would be 35 to 220 km in diameter (Whitehead and Luther, 1975); these are likely to be

61

compositionally driven diapirs (Hansen, 2003), which may result in a dampen effect of basin formation due to loss of thermal density. This indicates a minimum lithosphere thickness of 35 km in order for surface structures to form (Koch and Manga, 1996).

Circular lows share characteristics with coronae, including depressions surrounded by concentric fractures. The closely-spaced nature of concentric fractures indicate that they formed over a thin lithosphere throughout diapir emplacement.

Circular lows also display features inconsistent with diapiric features, such as the lack of radial fractures. Models predict deformation of the surrounding surface in the presence of regional differential stress during diapir emplacement (Withjack and Scheiner, 1982; Cyr and Melosh, 1993) [Fig. 16]. However, the circular lows studied herein appear in settings generally free of regional structures indicative of regional deformation and deviatoric stress. In addition, the features studied herein are circular rather than elliptical, indicating most isotropic stress fields. Only six circular lows display radial structures, representing a small percentage of the global dataset. Volcanic activity might explain the lack of radial features, but 75% of the circular lows also lack obvious lobate flows, surface expressions of volcanic activity. Radial fractures can extend beyond the interior, rim and annuli of a circular low and be preserved to some extent as in the cases of Qakma Corona (V-14) and Nalwanga Corona (V-16) [Fig. 13b]. In the remaining four circular lows with radial fractures, the fractures are concentrated within the basin interior, suggesting that the radial fractures formed late during or that they post-date the formation of circular low. Therefore it is hard to link the diapir evolution model as the only mode of formation for all circular lows.

Caldera Hypothesis

Caldera collapse is another endogenic process that could lead to coronae basin formation (Janes et al., 1992; Squyres et al., 1992; Stofan et al., 1992; Stofan et al., 1997; DeLaughter and Jurdy, 1997). Calderas are depressions formed due to the collapse of an underlying magma chamber during withdrawal of magma (Carrigan, 2000). Caldera diameters reflects the size of the collapsed magma chamber. Calderas should display surrounding volcanic flows associated with the evacuation and subsequent collapse of the underlying magma chamber. There are 97 features classified as calderas on Venus (Pace and Krassilnikov, 2003). Features identified as calderas on Venus display the following characteristics [Fig. 15b]: 1) circular to elongate depressions, 2) topographic rim, and 3) concentric fractures (Head et al., 1992; Barsukov et al., 1986; Krassilnikov et al., 2001; Squyres et al., 1992). These features range in diameter from 40 to 350 km with depths of 1 to 3 km. They display concentric extensional structures that occur from gravitational slumping of the caldera walls (63%), or both concentric and radial structures (36%) (Head et al., 1992). In addition they vary topographically from simple depressions (53%), to irregular flat shapes (11%), to depressions with low rims (6%). Calderas show debris from the wall collapse within the interior and show a smooth surface if flooding has occurred covering such debris. On Venus, calderas show little evidence of volcanic activity (Head et al., 1992; Krassilnikov and Head, 2004).

Evaluation of the Caldera Hypothesis

Some coronae with depressions have been interpreted to originate as calderas because of the common topographic depression and rims. For example, Colette Patera

and Sacajawea Patera in Lakshmi Planum (V-7) are interpreted as calderas (Roberts and Head, 1990). Calderas are circular to elongate shape surrounded by a topographic rim and annuli with depths of 1 to 3 km. The 47 circular lows that lack radial fractures can be compared to calderas. Circular lows are similar to calderas by being circular, with an interior depression, lacking radial fractures, and surrounded by an annulus. Circular lows also display characteristics different from calderas. Unlike calderas, circular lows form shallow depressions with depths ranging from 0.1 to 2.55 km. Aramaiti and Thouris have previously been considered possible calderas (Squyres et al., 1992; Stofan et al., 1992). However, detailed mapping of Aramaiti and Thouris by McDaniel (2005) led her to conclude that the features lack flooding to the extent expected, and are shallower in depths relative to calderas. Circular lows with deep basins are treated as outliers [Fig. 10a], ranging in depth from 1.65 km to 1.75 km. If circular lows are calderas, significant volcanic activity and flows are to be expected due to the magma chamber collapse. Ten circular lows display associated lobate flows. Three circular lows share both deep interiors and display lobate flows, Collete Patera and Sacajawea Patera (both in V-7) and Ledoux Patera (V-39). Roberts and Head (1990) have concluded from detailed mapping that both Collete Patera and Sacajawea Patera share characteristics similar to calderas. Ledoux Patera has a diameter of 72 km and displays volcanic flows that extend 20 times the surface area onto the surrounding areas. Ledoux Patera is also deep (1.75 km) with a rim typical of calderas. Therefore it is possible based on these basic observations that Ledoux Patera represents a caldera. However one must be cautious in accepting this interpretation, as the depth measurement could be an artifact due to the small diameter of Ledoux Patera. For two circular lows, the unnamed features in V-7 and V-22 (Un1 and

Un5 respectively) do not show major lobate flows associated with either of these features, which would be expected if they represent calderas. The smooth interiors in these basins are attributed to flooding of shields present all around the features. The depths of the remaining nine circular lows with volcanic flows range in depth from 0.2 to 0.8 km, much shallower than calderas. The interiors of circular lows range from smooth to rough surfaces, with fractures and folds attributed to regional stresses acting on the surface. The observed features indicate that circular lows do not likely represent calderas.

Impact Crater Hypothesis

Coronae have also interpreted as modified impact craters (Vita-Finzi et al., 2005; Hamilton, 2005). Impact craters are basins enclosed by circular rings (one or multiple), and surrounded by radial deposits of ejecta material in the exterior of the crater. Impact craters on Venus display low interiors (generally up to 1 km) surrounded by raised rims, concentric rings, ejecta blankets, and rarely, radar smooth or rough halos (Schaber et al., 1992; Ivanov et al., 1992; Sharpton, 1994; Herrick and Phillips, 1994). Impact craters, unlike diapir expressions on the surface, lack radial fractures. The surrounding surface is not structurally deformed [Fig. 15c]. Most Venusian impact craters are pristine, with less than 10% modified by volcanic or tectonic activity (Schaber et al., 1992). Erosion is cited as the major cause for ancient impact craters to be modified (Vita-Finzi et al., 2005; Hamilton, 2005). On Venus, however, lack of surface water and stable high atmospheric pressures make the rate of erosion very small and negligible (Arvidson et al., 1992). Coronae are interpreted as impact craters modified by: 1) wind erosion, 2) influence of the Venusian atmosphere over time, 3) endogenic processes such as diapirism, or 4)

volcanism triggered by the formative impact event (Hamilton, 2005; Vita-Finzi et al., 2005). The log-normal frequency distribution shows that impact crater and coronae size distribution are similar, although impact craters are, on average, smaller than coronae (Vita-Finzi et al., 2005). Variation in crater and coronae morphology depends on the modification of the craters.

Evaluation of the Impact Crater Hypothesis

A previous study of five circular lows by McDaniel (2005) suggested that these five circular lows formed via bolide impact on a rheological weak substrate. McDaniel (2005) noted the lack of radial fractures and close proximity of the five circular lows to ribbon-tessera terrain.

From this global study, we compare the characteristics of the 46 circular lows that lack radial structures, and are not caldera-like such as Collete Patera, Sacajawea Patera, and Ledoux Patera.

Circular lows share similar characteristics with impact craters including: 1) shallow depressions (less than 1.2 km); 2) rims; 3) concentric bands; 4) a lack of radial fractures; and 5) a lack of significant structural deformation in the surrounding areas. The aspect ratios of impact craters are compared to that of circular lows in Figure 18. From the log figure, it appears that aspect ratios for both impact craters (Herrick and Sharpton, 2000) and circular lows show similar trends, however circular lows are bigger and deeper compared to impact craters. The power law best fit equation for the aspect ratio of circular lows is: $d = 0.777 D^{-0.0667}$.
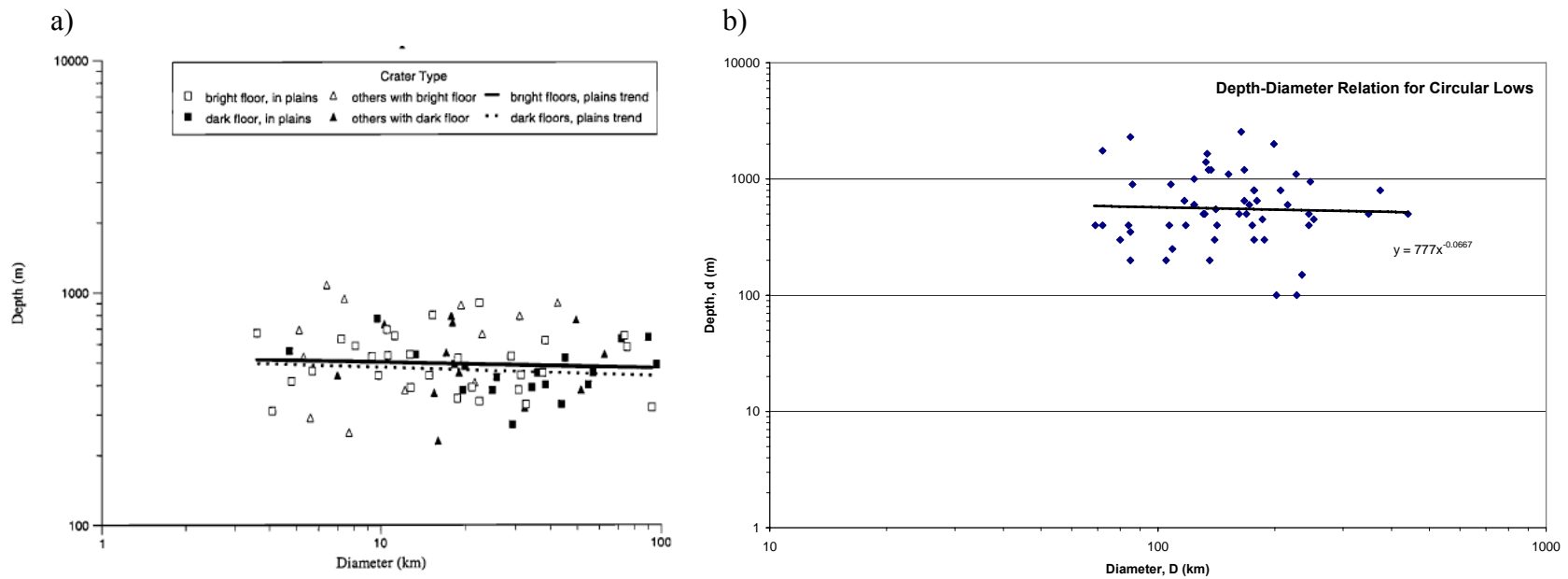
Figure 18. Log aspect ratio comparisons between impact craters and circular lows.
   a) The log aspect ratios for impact craters with varying crater morphologies on Venus (after Herrick and Sharpton, 2000).
   b) Log aspect ratios for circular lows show circular lows are bigger features yet similar in depths when compared to impact craters.

67

In the case of impact craters it was challenging to find a complete depth data set readily available in literature to determine the depth-diameter aspect ratio. Most sources only provide diameter values for all impact craters. According to Ivanov and Ford (1993); the depth (h) of the largest Venusian impact craters (70 km to 280 km) can be determined using the following equation: $h = 0.25d^{0.26}$, where d is diameter. Garvin and Schaber (1992) give a different equation to determine depths for impact craters greater than 80 km ($d = 0.063D^{0.60}$, where d is the impact crater depth and D is diameter). Garvin and Schaber (1992) also state that the depth-diameter aspect ratio values typically range from 0.007 to 0.015. In the case of circular lows, the depth-diameter aspect ratio values range from 0.0004 to 0.027, as calculated using data measurements recorded.

McDaniel (2005) modeled the erosion of the pristine impact crater Mead and compared it to her observations of five mapped circular lows. She concluded that the halo and ejecta around an impact crater would be first to erode, followed by the gradual disappearance of sharp contacts between the impact crater and surrounding surface. Circular lows are similar to the model eroded Mead in that they lack halos and ejecta deposits. The Mead model predicts the rim height to decrease with erosion or even erode completely with debris from the rim possibly filling the depression, making the rim wider with increasing erosion. Most circular lows display rims with heights reaching 1.6 km; however, the rims do not uniformly surround the circular lows in many cases and are also not uniform in width all around the circular low. Unlike the model of an eroded Mead crater interior, circular lows do not display debris that may have filled the depression with erosion. Fractures around an impact crater would be less defined with increasing erosion as predicted by the model. Sharp contacts between the edges of circular lows and

68

the surrounding surface are still intact unlike around eroded impact craters. Lack of

significant erosion on the surface to fill the interior of circular lows with debris, sharp

contacts, coupled with the variable rim heights make circular lows different from eroded

impact craters.   While circular lows could have formed by multiple processes, the

characteristics are consistent with forming by an impact process.

Tessera Terrain

If circular lows share characteristics with impact craters, it raises the question of why circular lows have not been classified as impact craters before. It may be that circular lows are either eroded impact craters or they represent impact craters that form on a rheologically different surface, for example on ribbon-tessera terrain. Therefore the location of circular lows to tessera terrain is recorded to determine any spatial relationship. Thirty circular lows lie in close proximity (within a diameter length around the circular low) to well-preserved ribbon-tessera terrain.

Ribbon-tessera terrain represent an ancient surface terrain that hosts ribbon and fold structures (Basilevsky and Head, 1998) and are proposed to represent solidified crust of cooling lava ponds that form crustal plateaus (Hansen, 2006). This introduces a different surface rheology that might lead to new sets of structures around features. Currently a global database of tessera terrain is being generated at the Planetary Processes Lab, University of Minnesota-Duluth using SAR and altimetry data (at 225 m/pixel and 275 m/pixel respectively).

Three hypotheses have been proposed and tested to determine the mode of formation of circular lows – namely the diapir, caldera, and impact crater hypotheses. Determining if circular lows have any relation to tessera terrain will allow a better evaluation on a mode of formation for circular lows.

The preservation of tessera terrain relative to circular lows is variable depending on the hypotheses. In the diapir mode, tessera terrain is likely to be modified or removed with increasing degree of regional stresses or structures associated with early dome formation. In the absence of regional stresses tessera terrain may be preserved, however

with volcanism being associated with diapir emplacements the absence of tessera is more likely due to burial from lobate flows. Of the six circular lows that display radial structures, only two (Qakma Corona in V-14 and Nalwanga Corona in V-16) lie adjacent to ribbon-tessera terrain.

With calderas, it is highly unlikely that much tessera terrain would be preserved in close proximity to circular lows due to the high degree of volcanism expected to be associated with calderas. All three circular lows proposed to be calderas are adjacent to ribbon-tessera terrain, however the coverage of ribbon-tessera terrain relative to circular low dimensions is being determined through independent mapping of tessera therefore this may change.

With the eroded impact craters hypothesis, it is likely that ribbon-tessera terrain adjacent to circular lows would also be modified due to the erosion. In her discussion, McDaniel (2005) noted that the pristine preservation of ribbon-tessera terrain surrounding circular lows, instead of being modified through erosion in accordance to the impact crater hypothesis. One explanation for the lack of erosion of ribbon-tessera terrain is due to its rheology. If tessera terrain had a weaker rheology at the time circular lows formed relative to its present rheology, it would explain how a bolide impact striking ribbon-tessera terrain might yield circular lows, with different characteristics compared to impact craters. With this in mind, it appears that circular lows might fit the "pristine" impact crater hypothesis with regard to structures observed. A cautionary note is that while circular lows lie close to ribbon-tessera terrain, the exact location of ribbon-tessera terrain with reference to circular lows has not been included in this study. Through independent detailed geologic mapping of some circular lows, there is evidence that small portion of

ribbon-tessera terrain might be preserved in the interior of circular lows (for example, Xcanill Corona in Agnesi (V-45), Hansen et al. (2008, unpublished)). In this case, the impact crater hypothesis would fail because materials pre-existing a bolide impact should be destroyed upon impact. Only through detailed mapping of individual circular lows can the issue of proximity to ribbon-tessera terrain be further addressed.

Alternative Hypotheses

The morphological characteristics of circular lows are not easily addressed by buoyant diapir rise, or caldera collapse. And the bolide impact hypothesis does not address the presence of tessera terrain within the basin interior of some circular lows. The following section outlines two new hypotheses for circular low formation. Both hypotheses involve subsidence through subsurface processes – by negatively buoyant diapirs and/or an evacuation process.

Negative Buoyancy Diapirs Hypothesis

Negative diapirs are negatively buoyant with respect to their surroundings. Consider a crust in which a dense material layer overlies a less dense material layer, the net buoyancy is greater in the denser layer and may be sufficient to cause the dense layer to sink [Fig. 15d]. On the surface this could result in a circular depression. The width of the depression could scale to the size of the negative diapir, layer thickness, and presumably layer strength. Concentric structures may develop on the surface if the underlying negative diapir reaches a level of neutral buoyancy and spreads laterally. All structures that exist on the surface directly above the sinking diapir would presumably be preserved even after the sinking event.

Material Evacuation or Drainage Hypothesis

An alternate process of subsidence is from the evacuation of a pre-existing magma reservoir within the crust [Fig. 15e]. A pre-existing magma chamber could start draining out the magma keeping the chamber outline intact. This process is analogous to

the appearance of sinkholes resulting from a subsurface drainage network resulting in a karst-like topography. Material evacuation is similar to a caldera collapse process however the material exists into the surrounding subsurface rather than being expelled to the surface. Unlike in the negative buoyancy diapir setting introducing an isostatic imbalance, material evacuation results in a spatial void. The overlying surface layer sinks without the subsurface material to support it. Surface expressions of this subsurface process might be analogous to the negative buoyancy diapir process. Observations include: 1) a circular feature with a size that scales to that of the underlying magma chamber, 2) shallow central depressions, and 3) possible concentric annuli along the edges. The size of the depression scales the size of the magma chamber. Similar to the negative diapir hypothesis, structures that exist on the surface before drainage of a magma chamber are still preserved post subsidence.

Both subsurface subsidence processes occur under different circumstances, yet on the surface a common set of structures and features are predicted making it difficult to assess which process might have occurred.

Evaluation of the two subsidence hypotheses

Subsidence processes predict circular features, assuming a circular or spherical negative diapir and a circular evacuation chamber, with an interior depression to form, and concentric structures along the edges. Not much is stated in the literature regarding the surface expressions of karst-like processes for a non-sedimentary unit. In the case of a negative diapir, it is assumed that the subsurface would be cold without a great geothermal gradient and therefore there is no volcanism associated with such a process.

With subsurface drainage, the evacuation is more permanent therefore is more likely to preserve any ribbon-tessera terrain that may be present. Volcanism is also possible. However there are many parameters that are unknown such as where does the drained go, whether drainage is in one direction or not, how deep can the chamber be located such that structures are still visible on the surface. More tests and models need to be undertaken in order to predict characteristic structures. On the basis that pre-existing structures will be preserved within the interior of the basin, one can justify the presence of tessera terrain within circular lows. The shallow depths that circular lows display may give clues to the extent of subsidence. These hypotheses are postulated and models have not been tested on circular lows as it is beyond the limits of this particular study. The subsidence models provide an alternative to the impact crater hypothesis to justify the presence of ribbon-tessera terrain in the circular low basin. Therefore a good starting place to test and compare results to the impact crater hypothesis will be in determining the location of tessera terrain relative to the interior of a circular low.

Summary

Circular lows are identified by their circular shape, amphitheatre like depressions, possible rim, concentric structures, and lack of radial fractures. The catalogued circular lows are inconsistent with the positive diapir and caldera hypotheses. Characteristics of circular lows are more consistent with characteristics of impact craters. Determining the position of ancient tessera terrain relative to circular lows is one way to test the impact crater hypothesis on all circular lows. Subsidence hypotheses provide alternative mechanisms for circular low formation.

Implications

Fifty-five circular lows represent 10% of coronae and display characteristics similar to those surrounding impact craters. If circular lows represent impact craters or a subsurface subsidence process, this affects our understanding of Venus. It questions the widely assumed view that all coronae form by a single mechanism – whether via an endogenic or exogenic process (Stofan et al., 1991, 1992, 1997, 2001; Squyres et al., 1992; Janes et al., 1992; Smrekar and Stofan, 1997; Vita-Finzi et al., 2005; Hamilton, 2005). This study also raises questions regarding the average model surface age of Venus (McKinnon et al., 1997), and how do structures characteristic of circular lows differ from structures associated with Venus' well documented impact crater database. I identified 55 circular lows that range in diameter from ~70 km to 441 km, with mean size of 163 km. In comparison, Venus has 970 impact craters with diameters from 1.5 to 279 km, and mean size of 20 km (Vita Finzi et al., 2005; Hamilton, 2005; McKinnon et al., 1997). Most impact craters are less than 60 km in diameter, unlike circular lows that are

mostly greater than 100 km. Such differences between the size of circular lows and impact craters will affect the densities of impact craters on the surface. Crater densities are used to determine the average surface age (McKinnon et al., 1997), therefore adding circular lows to the impact crater catalog will yield an older surface age of Venus than presently known. The results from this study also imply that the term coronae needs to be readdressed because circular lows are features previously identified as coronae.

If circular lows represent surface expressions of subsidence within the upper crust, this adds a new dimension to the list of endogenic processes and ways in which Venus loses internal heat.

Future Work

To further test both the impact crater and subsidence models, detailed geologic mapping of individual circular lows and the surrounding region is essential. Geologic mapping using high resolution images can assist in determining more accurately the annuli spacing, distance and height of tessera terrain adjacent to circular lows, and construct emplacement histories for circular lows. Modeling subsurface processes of subsidence and evacuation can better constrict surficial expressions and then be tested against observed structures associated with circular lows to determine if subsidence is a possible mode of formation for circular lows.

Spatial correlation of circular lows with coronae was determined using ArcGIS^{TM} and ArcGIS^{TM} Globe. However performing spatial correlation of circular lows with each other was not possible due to limitations in the software (the globe in ArcGIS^{TM} is set by default to Earth settings). Another limitation results from the fact that presently it is not

77

possible to stitch all individual quadrangles together to generate a single shapefile

(because quadrangles are projected in different projection systems) in order to conduct

any spatial analysis. Once the software specifications can accommodate various

planetary settings not only the Earth, and it is possible to stitch all 62 quadrangles

together; nearest neighbor analysis, cluster analysis, and spatial autocorrelation should be

performed for circular lows to determine any relevant spatial correlations.

It will be interesting to determine how circular lows fit with regards to the average mean

surface ages (AMSA) of the Venusian surface (Hansen and Young, 2007). This can be

accomplished once shapefiles of both the AMSA layer and the Venus quadrangles are set

to the same projection system.

Appendix

Foreshortening and Layover in Magellan SAR Images

The orientation of surface topography relative to the radar sensor has a pronounced effect on the brightness of radar images. In order to penetrate the thick CO_2 rich atmosphere, it was necessary to take side-view images of the surface rather than overview images so as to obtain maximum surface coverage [Fig. 4]. In this manner, features appear bright and spatially compressed if the terrain slopes toward the imaging sensor (Ford and Plaut, 1993; Chapman and Zimbleman, 1998). Terrain that slopes away from incident radar appears radar-dark and spatially expanded. The amount of distortion of topographic features depends on the relief and on the incidence angle between the sensor and the feature. Small incidence angles result in greater distortion for a given amount of topographic relief. Backscatter energy will reach the sensor quicker for high elevation areas relative to low elevation areas, causing the higher elevation area to be imaged at a position closer to the satellite than its actual position; a process called foreshortening. Similarly, a pulse from a high elevation returns to the sensor before a low elevation pulse, thereby creating a lay-over. Radar shadows of objects tilted away from the sensor at an angle greater than the incident angle tends to block out information of the surface (Ford and Plaut, 1993). Using separate left-look, right-look, or stereo imagery of the same area can partially address these concerns.

Surface roughness also plays a factor on how much energy from the surface is backscattered and captured by the sensor. Rough surfaces have a higher backscatter than smooth surfaces [Fig. 6] and there is a more sensitive response to the surface roughness with longer radar wavelength. Electrical properties of the imaged surface also play a

factor on image brightness. However, electrical properties are difficult to deconvolve

(Ford and Plaut, 1993).

References

Arvidson, R. E., Greeley, R., Malin, M. C., Saunders, R. S., Izenberg, N., Plaut, J. J., Stofan, E. R., and Shepard, M. K. (1992) Surface modification of Venus as inferred from Magellan observations of plains. *Journal of Geophysical Research*. **97**, No. E8, 13303-13317.

Barsukov, V.L., Volkov, V. P., and Khodakovsky, I. L. (1982) The crust of Venus; theoretical models of chemical and mineral composition. *Journal of Geophysical Research*. **87**, Suppl. B1, A3-A9

Barsukov, V. L. and 29 others. (1986) The geology and geomorphology of the Venus surface as revealed by the radar images obtained by Veneras 15 and 16. *Journal of Geophysical Research.* **91**, D378-D398.

Basilevsky, V.L., Pronin, A.A., Ronca, L.B., Kryuchkov, V.P., Sukhanov, A.L., and Markov, M.S. (1986) Styles of tectonic deformation on Venus: Analysis of Veneras 15 and 16 data. *Journal of Geophysical Research*. **91**, 399-411.

Basilevsky, A. T., and J. W. Head III. (1998) The geologic history of Venus: A stratigraphic view. *Journal of Geophysical Research*. **103**. No. E4. 8531–8544.

Batson, R.M., 1990, Cartography, *in* Greeley, Ronald, and Batson, R.M., Planetary Mapping: New York, Cambridge University Press, p. 60-95.

Bindschadler, D.L., and Head, J.W. (1991) Tessera terrain, Venus: Characterization and models for models for origin and evolution. *Journal of Geophysical Research*. **96**, 5889-5907.

Carrigan, C.R. (2000) Plumbing systems. In Houghton, B., McNuthg, S.R., Rymer, H., and Stix, J., *eds., Encyclopedia of Volcanoes.* San Diego, Academic Press, 219 – 235.

Chapman, M.G., and Zimbleman, J.R. (1998) Corona Associations and their implications for Venus. *Icarus*. **132**, 344-361.

Cyr, K.E., and Melosh, H.J. (1993) Tectonic patterns and regional stresses near Venusian coronae. *Icarus*. **102**, 175-184.

DeLaughter, J. E., and Jurdy, D. M. (1997) Venus resurfacing by coronae: Implications from impact craters. *Geophysical Research Letters*. **24**, 815-818.

Farr, T.G. (1993) Chapter 5. Radar interactions with geologic surfaces. *in* Ford, J.P., Plaut, J.J., Weitz, C.M., Farr, T.M., Senske, D.A., Stofan, E.R., Michaels, G., and

Parker, T.J. *eds*., *Guide to Magellan Image Interpretations*: Pasadena, JPL Publication **93-24,** 45-55.

Fink, J., Bridges, N.T., Grimin, R. (1993) Shapes of Venusian "Pancake" Domes imply episodic emplacement and silicic composition. *Geophysical Research Letter*. **20**, No. 4, 261-264.

Ford, J.P. (1993) Chapter 1. Magellan: the mission and the system. *in* Ford, J.P., Plaut, J.J., Weitz, C.M., Farr, T.M., Senske, D.A., Stofan, E.R., Michaels, G., and Parker, T.J. *eds*., *Guide to Magellan Image Interpretations*: Pasadena, JPL Publication **93-24**, 1-5.

Ford, J.P., and Plaut, J.J. (1993) Chapter 2. Magellan image data. *in* Ford, J.P., Plaut, J.J., Weitz, C.M., Farr, T.M., Senske, D.A., Stofan, E.R., Michaels, G., and Parker, T.J. *eds*., *Guide to Magellan Image Interpretations*: Pasadena, JPL Publication **93-24**, 7-18.

Gavin, J.B., and Schaber, G.G. (1992) Morphometry of large impact craters on Venus: Comparisons with terrestrial and lunar examples. *Lunar and Planetary Science Conference XXIII Abstracts*. **399**.

Ghent, R.R., and Hansen, V.L. (1999) Structural and kinematic analysis of eastern Ovda Regio, Venus: Implications for crustal plateau formation. *Icarus*. **139**, 116-136.

Glaze, L.S., Baloga, S.M. (2008) A new approach to inferences for pancake domes on Venus. *Lunar and Planetary Science Conference XXXIX Abstracts*. **1326**.

Hamilton, W.B. (2005) An Alternative Venus. *Philadelphia Annual Meeting Special Paper*. 1-76.

Hansen, V.L. and Willis, J.J. (1996) Structural analysis of a sampling of tesserae: implications for Venus geodynamics. *Icarus*. **123**, 296-312.

Hansen, V.L. and Willis, J.J. (1998) Ribbon terrain formation, southwestern Fortuna Tessera, Venus: implications for lithosphere evolution. *Icarus*. **139**, 116-136.

Hansen, V.L., Banks, B.K., and Ghent, R.R. (1999) Tessera terrain and crustal plateaus, Venus. *Geology*. **27**, 1071-1074.

Hansen, V.L., Phillips, R.J., Willis, J.J., and Ghent, R.R. (2000) Structures in tessera terrain: Issues and answers. *Journal of Geophysical Research*. **105**, 4135-4152.

Hansen, V.L., (2003) Venus diapirs: Thermal or compositional? *Geological Society of America*. **115**, 1040-1052

Hansen, V.L. (2006) Geologic constraints on crustal plateau surface histories, Venus: The lava pond and bolide impact hypotheses. *Journal of Geophysical Research*. **111**, E11010-11032.

Hansen, V.L., and Young, D. (2007) Venus's evolution: A synthesis. *Geological Society of America*. **Special Paper 419**, 255-273.

Hansen, V.L., and Lopez, I. (2008) Venus: No catastrophic resurfacing, no plate tectonics, but a rich ancient history – Results from global ribbon tessera terrain mapping. *Lunar and Planetary Science Conference XXXIX Abstracts*. **1644.**

Head, J (III)., Crumpler, L., Aubele, J., Guest, J., and Saunders, R. (1992) Venus Volcanism: Classification of Volcanic Features and Structures, Associations, and Global Distribution from Magellan Data. *Journal of Geophysical Research*. **97 (E8)**, 13153-13197.

Herrick, R.R., and Phillips, R. J. (1994) Implications of a global survey of Venusian impact craters. *Icarus*. **111**, 387-416

Herrick, R.R., Sharpton, V.L., Malin, M.C., Lyons, S.N., and Freely, K. (1997) Morphology and morphometry of impact crater. *in* Bouger, S.W., Hunten, D.M., and Phillips, R.J., *eds.*, Venus II: Tucson, University of Arizona Press, p. 1015-1046.

Herrick, R.R., and Sharpton, V.L. (2000) Implications from stereo-derived topography of Venusian impact craters. *Journal of Geophysical Research*. **105**, E8, 20,245 -20,262.

Ivanov, M.A., and Head, J.W. (1992) Tessera terrain on Venus: A survey of the global distribution, characteristics, and relation to surrounding units from Magellan data. *Journal of Geophysical Research*. **97**, 16,167-16,181.

Ivanov, M.A., and Ford, P.G. (1993) The depths of the largest impact craters on Venus. *Lunar and Planetary Science Conference XXIV Abstracts*. **689**.

Ivanov, M.A., and Head, J.W. (1996) Tessera terrain on Venus: A survey of the global distribution, characteristics, and relation to surrounding units from Magellan data. *Journal of Geophysical Research*. **105**, 11,171-11,183.

Izenberg, N.R., Arvidson, R.E., and Phillips, R.J. (1994) Impact crater degradation on venusian plains. *Geophysical Research Letters*. **21**, 4, 289-292.

Janes, D.M., Squyres, S.W., Bindschadler, D.L., Baer, G., Schubert, G., Sharpton, V.L., and Stofan, E.R. (1992) Geophysical models for the formation and evolution of coronae on Venus. *Journal of Geophysical Research*. **100**, 21,173-21,187.

Kirk, R.L., Soderblom, L.A., and Lee, E.M. (1992). Enhanced Visualization for Interpretaion of Magellan Radar Data: Supplement to the Magellan Special Issue. *Journal of Geophysical Research*. **85**, 8282-8294.

Koch, D.M., and Manga, M. (1996) Neutrally buoyant diapirs: a model for Venus coronae. *Geophysical Research Letters*. **23**, 225-228.

Krasilnikov, A.S., Galkin, V.A., Basilevsky, A. T. (2001) Tectonics and Evolution of Coronae on Venus: Preliminary Results of Tectonophysical Modeling. *Solar System Research*. **35**, No. 2, 103-116

Krassilnikov, A.S. and Head, J. (2004) Calderas on Venus and Earth: Comparison and models of Formation. *Lunar and Planetary Science Conference Abstracts*. **1531.**

Longley, P.A., Goodchild, M.F., Maguire, D.J., and Rhind, D.W. (2005) Chapter 5. Georeferencing. *in* Geographic Information Systems and Science, John Wiley and Sons Publications, p. 110-126.

McDaniel, K.M. (2005) Circular Lows. A genetically distinct subset of coronae on Venus? M.S. Thesis. University of Minnesota-Duluth press. 1-79.

McKinnon, W.B., Zahnle, K.J., and Melosh, H.J. (1997) Cratering on Venus: models and observations. *In* Bouger, S.W., Hunten, D.M., and Phillips, R.J., *eds., Venus II:* Tucson, University of Arizona Press. 969-1014.

Okubo, C.H., and Martel, S.J. (1998) Pit crater formation on Kilauea Volcano, Hawaii. *Journal of Volcanology and Geothermal Research*, **86**, No. 1-4, 1-18.

Pace, K.R., and Krassilnikov, A.S. (2003) Calderas on Venus: Tectonics, Volcanism and Relationship with Regional Plains. *Lunar and Planetary Science Conference XXXIVAbstracts.* **1309.**

Pavri, B., Head, J., Klose, K., Wilson, L. (1992) Steep Sided Domes on Venus: Characteristics, Geologic Setting and Eruption Conditions From Magellan Data. *Journal of Geophysical Research.* **97**, E8, 13445-13478.

Phillips, R.J., Raubertas, R.F., Arvidson, R.E., Sarkar, I.C., Herrick, R.R., Izenberg, N.R., and Grimm, R.E. (1992) Impact craters and Venus resurfacing history. *Journal of Geophysical Research*. **97**, 15,923-15,948.

Phillips, R.J. and Hansen, V.L. (1994) Tectonics and magmatic evolution of Venus. *Annual Review of Earth and Planetary Science.* **22**, 597-654.

Phillips, R.J., and Izenberg, N.R. (1995) Ejecta correlations with spatial crater density and Venus resurfacing history. *Geophysical Research Letters*. **22**, 1517-1520.

Plaut, J.J. (1993) Chapter 3. The non-SAR experiments. *in* Ford, J.P., Plaut, J.J., Weitz, C.M., Farr, T.M., Senske, D.A., Stofan, E.R., Michaels, G., and Parker, T.J. *eds*., *Guide to Magellan Image Interpretations*: Pasadena, JPL Publication 93-24, p.19-31.

Plaut, J.J. (1993) Chapter 4. Stereo Imaging. *in* Ford, J.P., Plaut, J.J., Weitz, C.M., Farr, T.M., Senske, D.A., Stofan, E.R., Michaels, G., and Parker, T.J. *eds*., *Guide to Magellan Image Interpretations*: Pasadena, JPL Publication 93-24, p.33-43.

Roberts, K.M., and Head, J.W. (1990) Lakshmi Planum, Venus: Characteristics and Models of Origin. *Earth, Moon, and Planets*. **50/51**, 193-249.

Saunders, R.S., Pettengill, G.H., Arvidson, R.E., Sjogren, W.L., Johnson, W.T.K, and Pieri, L. (1990) The Magellan Venus Radar Mapping Mission. *Journal of Geophysical Research*. **95**, B6, 8339-8355.

Saunders, R.S., and 26 others. (1992) Magellan Mission Summary. *Journal of Geophysical Research*. **97**, 13,067-13,090.

Schaber, G.G., Strom, R.G., Moore, H.J., Soderblom, L.R., Kirk, R.L., Chadwick, D.J., Dawson, D.D., Gaddis, L.R., Boyce, J.M., and Russell, J. (1992) Geology and the distribution of impact craters on Venus: What are they telling us? *Journal of Geophysical Research*. **97**, 13,257-13,301.

Sharpton, V.L. (1994) Evidence from Magellan for unexpectedly deep complex craters on Venus. *Geological Society of America*. **Special Paper 293**, 19-27.

Smrekar, S.E., and Stofan, E.R. (1997) Corona formation and heat loss on Venus coupled by upwelling and delamination. *Science*. **277**, 1280-1294.

Squyres, S.W., Janes, D.M., Baer, G., Bindschadler, D.L., Schubert, G., Sharpton, V.L., and Stofan, E.R. (1992) The morphology and evolution of coronae on Venus. *Journal of Geophysical Research*. **97**, 13,611-13,634.

Stofan, E.R., Bindschadler, D.L., Head, J.W., and Parmentier, E.M., (1991) Corona structures on Venus: Models of Origin. *Journal of Geophysical Research*. **96**, 20,933-20,946.

Stofan, E.R., Sharpton, V.L., Schubert, G., Baer, G., Bindschadler, D.L., Janes, D.M., and Squyres, S.W. (1992) Global distribution and characteristics of coronae and related features on Venus: Implications for origin and relation to mantle processes. *Journal of Geophysical Research*. **97**, 13,347-13,378.

Stofan, E.R., Hamilton, V.E., Janes, D.M., and Smrekar, S.E. (1997) Coronae on Venus: morphology and origin. *in*. Bouger, S.W., Hunten, D.M., and Phillips R.J., *eds*., Venus II: Tucson, University of Arizona Press, p. 931-965

Stofan, E.R., Smrekar, S.E., Tapper, S.W., Guest, J.E., and Grindrod, P.M. (2001) Preliminary analysis of an expanded corona database for Venus. *Geophysical Research Letters*. **28**, 4267-4270.

Tanaka, K.L. (2003) Magellan Data Products: The Venus Geologic Mappers' Handbook, *U.S. Geological Survey*. (http://astrogeology.usgs.gov/Projects/PlanetaryMapping/VenusMappers/VGM_Handbook_94.pdf)

Vita-Finzi, C., Howarth, R.J., Tapper, S.W., and Robinson, C.A. (2005) Venusian craters, size distribution, and the origin of coronae. *Geological Society of America.* **Special Paper 388**, 815-823.

Whitehead, J.A. and Luther, D.S. (1975) Dynamics of laboratory diaper and plume models. *Journal of Geophysical Research*. **80**, 705-717.

Withjack, M., and Scheiner, C. (1982) Fault patterns associated with domes- an experimental and analytical study. *The American Association of Petroleum Geologists Bulletin*. **66**, 3002-3016.

Zimbelman, J.R. (2001) Image resolution and evaluation of genetic hypotheses for planetary landscapes. *Geomorphology*. **37**. 179-199.
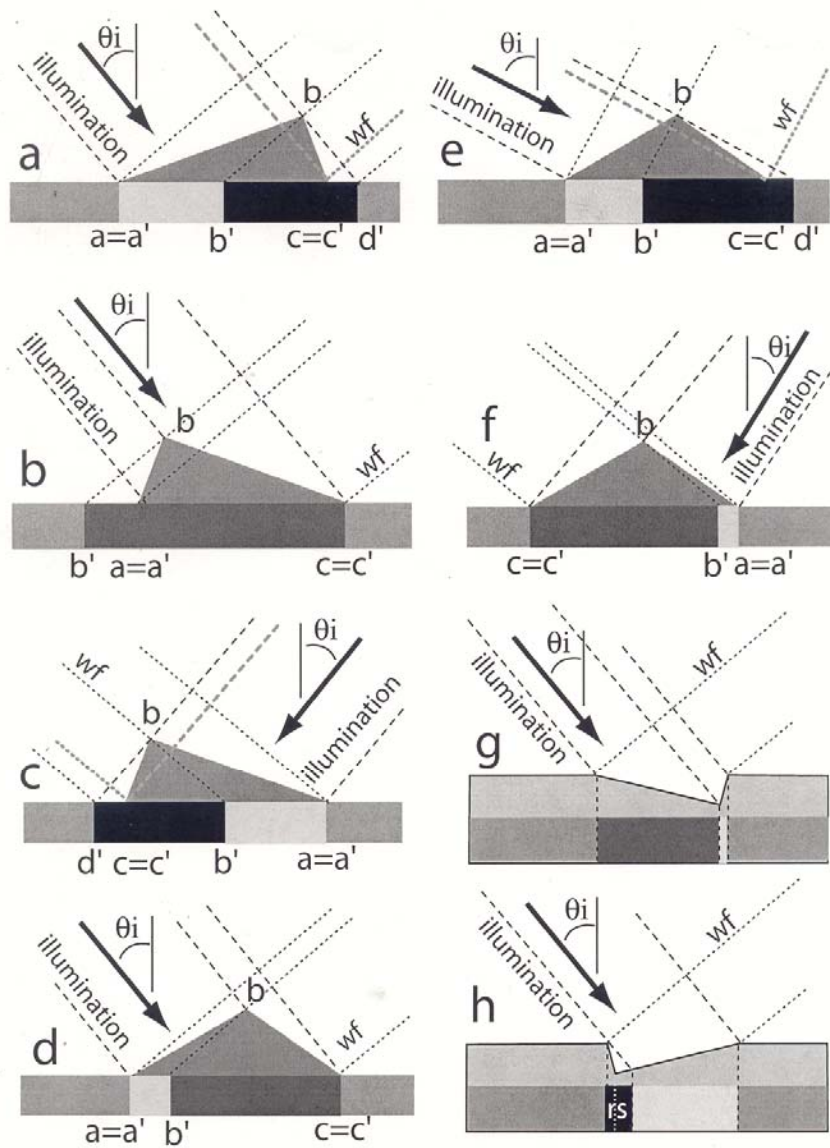
Figure 19. Various combinations (a – h) of foreshortening and layover in cross-view with different incident angles and look directions. Regions that face away from the sensor appear radar dark and spatially expanded. The total amount of distortion of a surface depends on the elevation and incidence angle of sensor. Grey shades indicate the degree of radar brightness (Hansen through personal communication- after Tanaka et al; ask HER FOR THE REFERENCE) Need to explain to the reader how to interpret the diagrams.